Lab on a Chip

PAPER

View Article Online
View Journal

Cite this: DOI: 10.1039/d5lc00703h

Hydrophilic skin-interfaced microfluidic devices for comprehensive sweat collection and analysis

Fina Lu,† Ji Hyun Yang † and Ahyeon Koh *

Blood and interstitial fluids are standard biofluids for clinical assessments. Despite their rich analyte content, the adaptation of bioanalysis in wearable devices limits its use because their collection requires invasive procedures. In contrast, sweat contains many of the same biomarkers found in blood, offering a non-invasive alternative for health monitoring. However, the relationship between sweat composition, gland physiology, and their clinical relevance remains poorly understood. To evaluate the feasibility of sweat as a reliable biofluid for health monitoring, it is essential to examine the mechanisms of biomarker diffusion and their correlation between blood and sweat glands, employing rigorous analytical methodologies. Recent research has increasingly emphasized accurate and precise detection of metabolites, proteins, and disease-specific biomarkers in sweat for applications in clinical diagnostics, preventive healthcare, and early disease detection. Thus, soft skin-interfaced polydimethylsiloxane (PDMS)-based microfluidic devices have recently emerged as promising platforms for on-demand sweat biomarker analysis. However, the intrinsic hydrophobicity of PDMS poses a limitation by hindering efficient sweat transport through microfluidic channels, necessitating specific pressure thresholds for optimal collection, presenting a significant challenge for reliable sample collection and analysis in sweat-based health monitoring. This work introduces a hydrophilic, skin-interfaced microfluidic device fabricated using a composite material of block copolymer PDMS–polyethylene glycol (PDMS–PEG) and PDMS to address the intrinsic material challenges. The hydrophilic modification significantly enhances the ease of sweat harvesting, particularly during the initial sweating event, enabling more comprehensive capture of molecular information compared to traditional PDMS-based devices. Comprehensive characterization of the microfluidic devices demonstrates improved surface properties, mechanical strength, optical clarity, and microfluidic performance. Integrating hydrophilic block copolymers into wearable sweat microfluidic systems enhances the potential for non-invasive platforms for reliable and rigorous health monitoring and paves the way for future clinical and occupational health applications.

Received 15th July 2025,
Accepted 15th October 2025

DOI: 10.1039/d5lc00703h

rsc.li/loc

Introduction

Wearable biosensors have seen rapid advancements in the past decade due to their health monitoring capabilities for telehealth care.[1–4] Current wearable devices predominantly monitor simple physiological metrics such as heart rate and physical activity, and they are not yet certified for medical use and lack the ability to provide deeper molecular insights.[5,6] This limitation has spurred the development of sensors capable of detecting physiochemical biomarkers in accessible biofluids.[7] Blood and interstitial fluid (ISF) serve as the standard biofluid for health monitoring; however, their invasive collection methods are unfavorable for daily monitoring and wide public distribution with ease of use. Although tears can be collected non-invasively, the process may cause discomfort and trigger reflex tearing, potentially distorting sensor readings. Additionally, the clinical significance of different types of tear fluids is not yet fully understood. Urine-based sensors are incompatible with continuous wearable formats. Saliva analysis provides limited clinically reliable physiological data, as it is heavily influenced by recent food intake and bacterial composition. Hence, sweat is an attractive biofluid, as recent studies suggest a linear correlation between sweat and blood analytes, combined with its ease of accessibility in daily monitoring.[8] The human body contains three primary types of sweat glands: eccrine, apocrine, and sebaceous glands. These glands are influenced by local interstitial fluids through passive diffusion, though each functions independently within its respective organ system.[8–12] The anatomical proximity of

Department of Biomedical Engineering, State University of New York at Binghamton, Binghamton, NY 13902, USA. E-mail: akoh@binghamton.edu
† These authors contributed equally to this work and shared first authorship.

sweat glands to the dermal capillary network facilitates the passive diffusion of blood-derived constituents into sweat, making sweat a rich and accessible source of biomarkers for health monitoring.[11,13] Sweat contains a variety of metabolites and volatile compounds, which offer valuable insights into metabolic and physiological processes.[14] For example, glucose concentrations in sweat are useful for monitoring glycemic control, with potential applications in diabetes management.[15] Lactate levels serve as an indicator of anaerobic respiration and physical exertion, while cortisol provides insight into the body's response to stress.[16,17] Additionally, larger metabolites such as proteins can offer insights into disease signaling pathways and physiopathological processes, helping to better understand the development and progression of various diseases. Inflammatory markers present in sweat, such as cytokines, are essential for assessing immune system activity and inflammation. This range of physiochemical biomarkers present in sweat highlights its potential for comprehensive health monitoring and assessing systemic health conditions pre- and post-diagnosis. Specifically, there is growing interest in low concentration sweat analysis and using targeted biomarkers beyond general metabolites as an alternative solution for clinical analysis, preventive medicine, and early medical screening.[16] However, the relationship between sweat biomarkers, gland systems, and their clinical significance is still poorly understood as a function of various secretion stages and physiological regulation mechanisms. Therefore, it is important to rigorously, quantitatively analyze biomarkers and understand the biomarker diffusion mechanism between blood and sweat glands to evaluate the accurate clinical relevance and potential of sweat as a biofluid for reliable health monitoring.[10] Recently, the collection and analysis of sweat has made significant progress due to innovative breakthroughs in 3D skin-interfaced soft microfluidics. Wearable microfluidic devices utilize microfluidic systems to manipulate fluids within channels that are at the tens to hundreds of micrometer scales, allowing onsite or on-demand analysis of sweat biomarkers.[18] Silicone elastomer polydimethylsiloxane (PDMS) is a foundational material used in soft lithographically defined wearable microfluidics, adapting engineering approaches in lab-on-a-chip to become lab-on-skin systems.[13,19,20] PDMS possesses a multitude of highly advantageous properties, such as unparalleled gas permeability, remarkable skin conformability, complete transparency, effortless microfabrication, exceptional bio-inertness, and affordability.[21] However, PDMS is inherently hydrophobic, which hinders wetting and impedes the transport of sweat within the microfluidic channels to integrated sensors. While this hydrophobicity can enable slow-paced sweat collection for accurate flow rate monitoring and the use of capillary burst valves in multi-reservoir systems, it also results in high channel impedance, particularly at the inlets.[22] This necessitates substantial sweat production, limiting the application of these systems to clinical or infrequent settings, especially for collecting isotonic priming sweat. Modifying PDMS to be hydrophilic can facilitate fluid flow in microfluidic devices and potentially lower the pressure threshold needed for sweat transport, pursuing sweat harvesting with minimal to no exercise during stimulation. Several approaches have been explored to address the hydrophobic nature of PDMS, including treatment of the surface with high energy using O_2 plasma, UV/ozone treatments, and corona discharges for the oxidation of the PDMS surface (Table S1). Plasma treatment is one of the most widely used methods, as it temporarily increases surface hydrophilicity by introducing polar functional groups onto the PDMS surface. However, plasma-induced hydrophilicity gradually diminishes over time due to the inherent hydrophobic recovery of PDMS, limiting its long-term utility in wearable applications. Alternative strategies such as chemical coatings and surface grafting of hydrogel or hydrophilic polymers like polyethylene glycol (PEG) have been proposed to impart more durable surface modifications.[23–26] A primary challenge in wearable sensing is the collection of sweat at low secretion rates typical of sedentary or resting conditions, which requires innovative material and device solutions.[3,7,11,27,28] To address this, many state-of-the-art platforms have incorporated hydrogels to actively draw sweat from the skin. For example, the work by Saha *et al.* demonstrates an elegant platform that uses an osmosis-driven hydrogel to actively extract sweat for continuous glucose monitoring at rest, with a particular focus on the fingertip due to its high sweat gland density.[29,30] Similarly, Nyein *et al.* developed a patch using hydrophilic fillers and a thin hydrogel layer to reduce dead volume and enable the rapid analysis of thermoregulatory sweat, also validated on the finger.[31] While these hydrogel-based approaches are powerful, they can introduce challenges such as fabrication complexity or potential sample dilution, which motivates the exploration of other material strategies.

Beyond the collection mechanism, the development of robust, standalone stretchable device platforms is a key area of research. The work by Cho *et al.* showcases an adhesive-free, stretchable microfluidic band that highlights the importance of device mechanics for a stable skin interface during exercise.[16] For long-term monitoring, Shin *et al.* have developed sophisticated bioinspired systems with features like Janus membranes and graded microchannels to enable multiday sweat sampling after a single stimulation session.[32] A common thread in these advanced platforms is the critical need for hydrophilic surfaces to effectively manage low sweat volumes. This remains a central challenge, as foundational materials like PDMS are inherently hydrophobic, and common surface treatments like plasma offer poor long-term stability

due to hydrophobic recovery. Recent state-of-the-art wearable sensors have successfully used PEG–PDMS composites to form hydrophilic microfluidic channels. For example, the work by Lorestani *et al.* on advanced lactate and glucose sensors utilized a PEG–PDMS composite as the structural material for their fluidic networks, which were then often plasma-treated to enhance surface wettability.[33,34] In those important studies, PEG–PDMS served as a key component to support the primary innovations in either active sweat uptake *via* hydrogel scaffolds or novel electrochemical sensor design. However, a systematic study of the PEG–PDMS material itself, and how fabrication conditions can be optimized to achieve stable hydrophilicity without secondary treatments, has not been fully explored. Moreover, there has yet to be a foundational, material-centric investigation that clearly illustrates how to optimize the PEG–PDMS composite for stable and passive sweat collection.

In this study, we introduce a skin-interfaced microfluidic device constructed from a composite of block copolymer (BCP) PDMS–polyethylene glycol (PDMS–PEG) and PDMS to address the intrinsic material challenges of PDMS.[25] The 3D hydrophilic, soft sweat harvesting system is developed using a simple, one-pot soft lithography technique with PDMS–PEG block copolymers. Microfluidic devices have been thoroughly tested and characterized for their surface properties, mechanical strength, optical clarity, and microfluidic performance. Hydrophilic skin-interfaced devices significantly improved the efficiency of sweat harvesting, particularly during the initial sweating event, and enhanced the reliability and rigor of quantitative sweat analysis compared to traditional PDMS sweat devices. Collecting reliable sweat samples without the need for intense physical activity is essential for effective sweat monitoring. This significant advancement facilitates progress in non-invasive sweat analysis and presents a

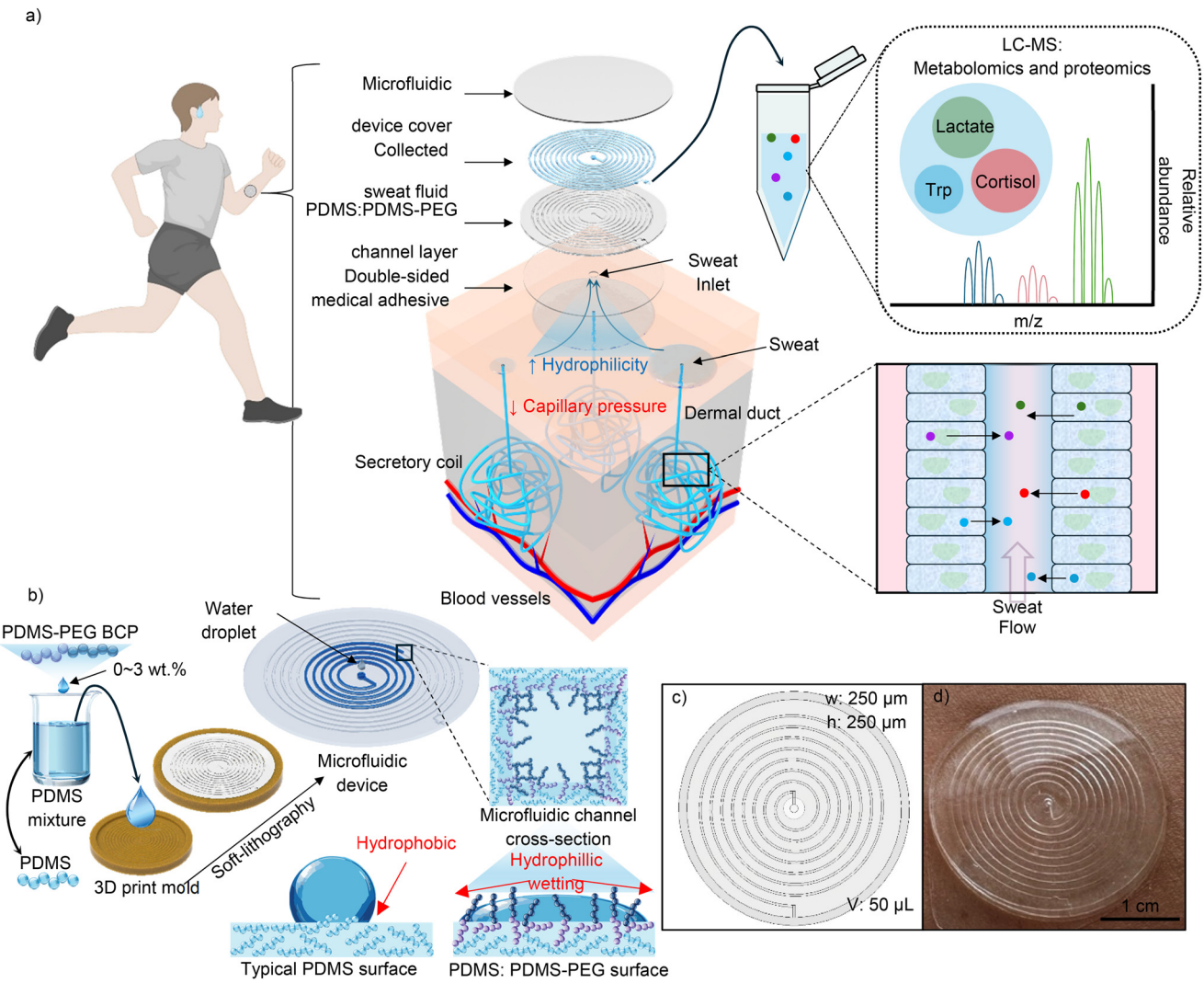

Fig. 1 Schematic overview of PDMS–PEG microfluidic device design, fabrication, and measurement strategy. (a) Conceptual illustration of the device showing sweat collection and biomarker analysis workflow using LC-MS. (b) Fabrication process of PDMS:PDMS–PEG films and microfluidic channels through soft lithography using 3D-printed molds. (c) Schematic of the microfluidic channel layout and its fluid capacity. (d) Photograph of the microfluidic device applied to the skin for on-body sweat collection.

multitude of potential applications that necessitate hydrophilic 3D soft bioelectronics systems.

Results and discussion

Fabrication of the hydrophilic skin-interfaced microfluidics for sweat collection

The hydrophilic sweat collection device adheres to the established design principles for skin-interfaced sweat sensors, also known as epifluidics.[1] The material selection and design strategies aim to ensure secure attachment to the skin while effectively harnessing perspiration pressure from sweat glands. These strategies also mitigate delamination caused by mechanical movement.

The schematic diagram (Fig. 1a) illustrates the soft microfluidic device mounted on the skin. Sweat, containing physiochemical biomarkers originating from the blood capillaries near the sweat glands, enters through the central opening of the medical adhesive, which also secures the device to the skin.[6,27,35] This central inlet connects to the fabricated PDMS–PEG device, which incorporates a microchannel designed to collect and transport sweat. The process is driven by the natural pumping pressure of the sweat glands (1–2 kPa) and capillary force inherent to the PDMS–PEG structure. The fabrication process (Fig. 1b) facilitates the efficient and straightforward fabrication of hydrophilic sweat collection microfluidics using a PDMS: PDMS–PEG composite. In this simple one pot process, PDMS–PEG BCP is mixed with uncured PDMS before following the standard soft-lithography protocol. A planetary centrifugal mixer was employed to effectively mix the two polymeric matrices in a homogenous state. To further reduce production costs and promote rapid prototyping, 3D-printed microfluidic molds define the microchannels, and a bar coating system applied to create thin and uniform PDMS–PEG films on the flat PI films to enclose the channels. The resulting microfluidic channel features a rectangular cross-section measuring 250 μm by 250 μm (Fig. 1c), capable of holding up to 50 μL of sweat fluid. This optimized design improves sweat retention for analysis, similar to the current gold standard sweat collection device (*i.e.*, Macroduct®). Soft microfluidic platforms offer several key advantages over traditional sweat collection methods. Their compact and lightweight design enables unobtrusive, skin-conformal integration, ensuring minimal interference with the wearer's natural activity. The flexible architecture accommodates diverse anatomical sites, allowing deployment across various body locations without compromising functionality (Fig. 1d). Additionally, the absence of rigid structural components improves wearer comfort and reduces motion artifacts, supporting accurate, continuous biosampling in real-world environments. Harvested sweat samples can be easily collected using a conventional autopipette and analyzed through sophisticated instrumental techniques such as LC-MS to evaluate a wide range of biomarkers. Furthermore, the harvested sweat can be efficiently retrieved from the device, with an extraction efficiency exceeding 99% using a standard laboratory micropipette (Fig. S1).[12] Although this is beyond the scope of the current manuscript, the platform has the potential to be integrated with on-site analytical measurements, including electrochemical sensing,[36] colorimetric analysis,[22] molecular imprint polymer detection,[37] and spectroscopic analysis.[38,39]

Surface characterization of the PDMS:PDMS–PEG block copolymer composite

The PDMS:PDMS–PEG block copolymer composite was systematically evaluated for its hydrophilicity as a function of mixing ratio and preparation methods. The surface tension of a material used in a microfluidic device significantly influences the threshold pressure required for biofluid harvesting and the capillary action force at the inlet. The PDMS:PDMS–PEG fabrication employed the conventional soft lithography technique, where the PEG block copolymer was added as an additive during PDMS formulation. This modification enhances the hydrophilic characteristics of the resulting material corresponding to the hydroxyl group in polyethylene glycol (PEG) repetitive units. This termination functional group contributes precise fluid control and improved wettability in microfluidic channels. Fig. 2 presents a comprehensive evaluation of the water contact angles (WCAs) of the composite film by varying the concentration of PEG block copolymers by weight percent within the PDMS matrix. We explored the interfacial effects during the curing of composite materials, as the state of the interfacial phase influences the reorganization of the block copolymer. The water contact angles were measured at both the top and bottom interfaces of PDMS:PDMS–PEG in contact with polyimide (PI) surfaces and air, respectively, as a function of PDMS–PEG block copolymer additives (Fig. 2a and b). The chemical structure orientation in the composite film is driven by the surface segregation of amphiphilic copolymers and the PDMS–PEG block copolymer within the PDMS matrix.[25] During thermal curing, the hydrophobic segments remain embedded in the PDMS, while the hydrophilic PEG segments migrate toward the surface, creating a stable hydrophilic layer.[25] Unmodified PDMS surfaces displayed a WCA of ~105° on both air- and PI-contacted interfaces. Increasing the PEG wt% decreased the overall WCA measurements of the PDMS:PDMS–PEG material. Notably, the bottom surface interfaced with PI exhibited a more significant decrease in WCA compared to the top surface interfaced with air. We hypothesized that the difference in surface tension is due to the migration of amphiphilic copolymers to the surface driven by thermodynamic forces,[25] rather than by gravitational force. The hydrophilic PEG segments tend to orient toward the surface, seeking interactions with the surrounding environment, which exhibits lower surface tension at the interface. It is noteworthy that, as shown in Fig. 2b, there is no significant difference in the WCA by sandwiching PI films during the curing process of the

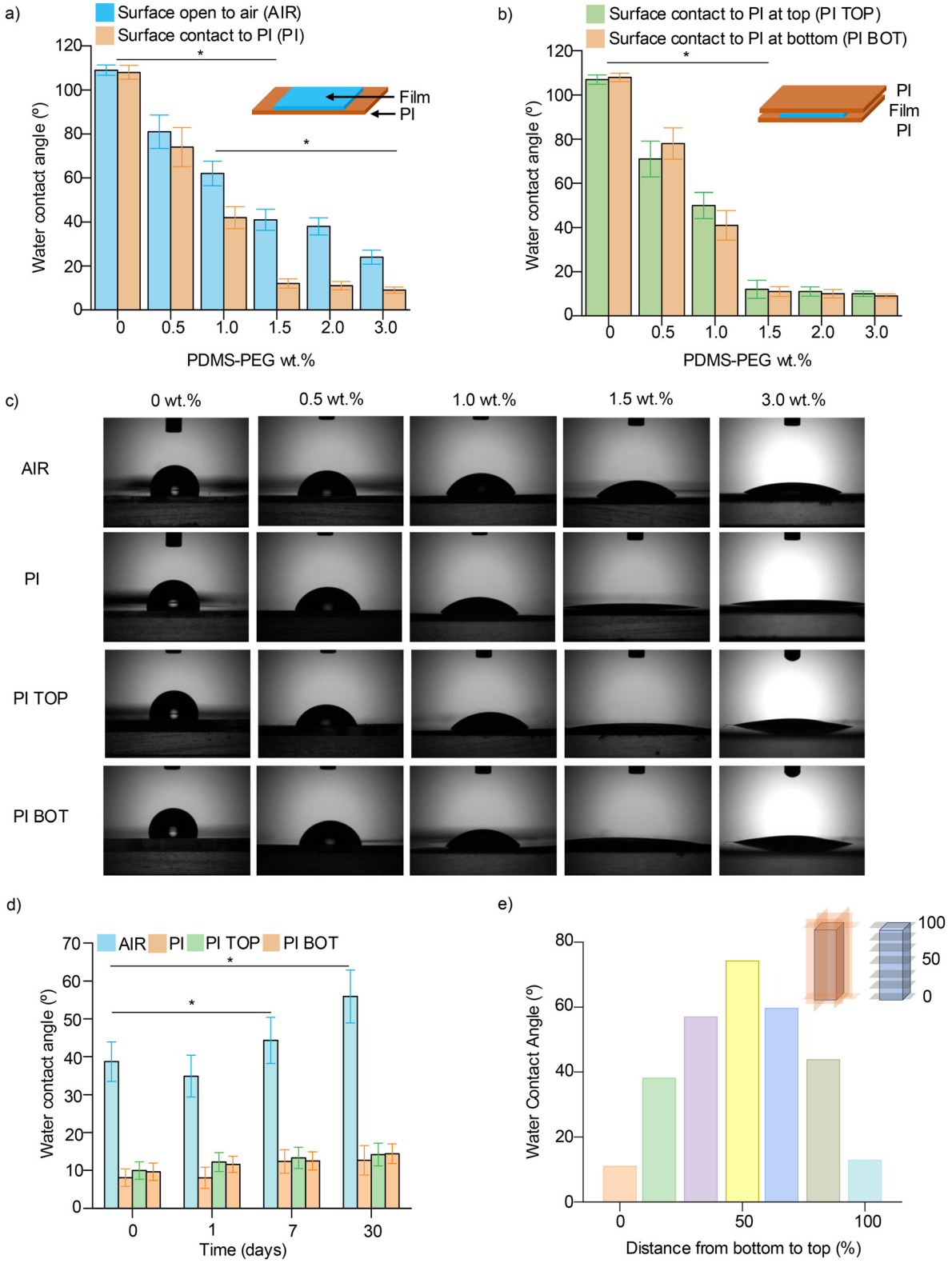

Fig. 2 Water contact angle assessment of PDMS and PDMS:PDMS–PEG films at various PEG wt% concentrations. WCA measurements of (a) AIR/PI and (b) PI TOP/PI BOT interfaces for PDMS and PDMS:PDMS–PEG films. Statistical analysis was performed using a paired *t*-test (black) for within PEG wt% levels (n = 5, $*p < 0.05$) and the Games–Howell *post hoc* test (respective color) for between groups (n = 5, $*p < 0.05$). Each inset image on the graph illustrates the naming conventions based on the film applicator method used during fabrication. (c) Representative WCA snapshots of the AIR/PI and PI TOP/PI BOT interface for PDMS and PDMS:PDMS–PEG films at 1 minute. (d) Long term WCA study of 1.5 wt% PDMS:PDMS–PEG films for both AIR/PI and PI TOP/PI BOT. Statistical analysis was performed using the Games–Howell *post hoc* test (n = 5, $*p < 0.05$). (e) *Z*-direction WCA measurements of a 1.5 wt% PDMS:PDMS–PEG rectangular slab at 1 minute, prepared using the PI TOP/PI BOT configuration (illustrated in the inset).

PDMS:PDMS–PEG composite film. These phenomena became more evident at a concentration of 1.5 wt% PDMS–PEG in the PDMS matrix (Fig. 2c). The chemical surface characteristics of the polymeric interface exhibited minimal influence on variations in the water contact angle. Comparative analyses using substrates such as polystyrene (PS), polycarbonate (PC), and polyethylene terephthalate (PET) against PI revealed no statistically significant differences in contact angle measurements across varying PDMS–PEG wt% (Fig. S2). PI is selected for further device fabrication due to its low cost, widespread availability, and thermal stability. Since the variation in performance among substrates was minimal and PI met practical manufacturing criteria, it was deemed the most suitable material for continued development of the PDMS-based microfluidic system.

Water contact angles (WCAs) were measured over time to study the hydrophobic recovery of a 1.5 wt% PDMS:PDMS–PEG film. As shown in Fig. 2d, the PDMS:PDMS–PEG film that was exposed to air during the curing process gradually regained its hydrophobicity, resulting in a 15° increase in the WCA in a month. In contrast, the other films that were in contact with PI exhibited minimal changes, retaining WCAs with only a roughly 5° increase after one month, which is a statistically insignificant change. The composite film, when cured with the PI film interface, managed to retain wettability over time, making it the optimal choice for biomedical applications and commercial viability. While these results confirm the long-term stability of the material's key surface property in an aqueous environment, this study is limited to investigating the specific long-term chemical effects of salts and other electrolytes present in sweat. Therefore, future work will focus on rigorous testing of both the surface's chemical stability after prolonged exposure to saline biofluids and the integrated device's structural integrity and fluidic performance over days and weeks to fully validate it for long-term applications. The unique stability in surface characteristics of this polymer composite surpasses those of air-interfaced films and other reported PDMS and PDMS composites. The three-dimensional arrangement of the amphiphilic block copolymer in the elastomer polymeric matrix, as demonstrated by contact angle measurements in *z*-directions, exhibits the highest WCA in the middle of the composite matrix interacted with PI film interfaces (Fig. 2e). The variations in WCA characteristics along the vertical direction of the composite materials (rectangular block of 1 cm width by 1 cm length by 2.5 cm height) indicate that PEG segments are primarily located at the edges of the films rather than in their center.[40] Additionally, the wettability of the surface interacting with polymeric films exhibits greater kinetics than that observed in the middle of the film (Fig. S3).

This distinctive feature makes it well suited as a material for 3D skin-interfaced hydrophilic soft electronics, microfluidics, and various biomedical engineering studies. For example, it's long-term stability with consistent surface modification methods enhances the biocompatibility of the device, improving cell adhesion and supporting laminar flow in microfluidic-based bioengineering studies (*e.g.*, organ-on-a-chip). Specifically, the presence of a hydrophilic channel and interface around the inlet of the microfluidic device facilitates efficient liquid movement towards the inlet, aided by capillary force. This design not only ensures a smooth flow into the microfluidic device for collection, but also significantly reduces the pressure threshold for inlet burst, demonstrating the effectiveness of the sweat collection research and further benefiting clinical sweat analysis. This fabrication process is notable for its simplicity and use of less toxic precursors and greater compatibility and simplicity compared to the surface grafting strategies typically used in organosilane self-assembly methods within the field of microfluidic engineering.

Given the significant improvement in surface hydrophilicity observed at the 1.5 wt% PEG concentration, the microfluidic device fabrication in this study was based on this concentration. This choice is based on the advantages of a stable, hydrophilic microfluidic surface and the manufacturability of soft lithography.

To investigate the influence of topographical structures during the curing of the PDMS:PDMS–PEG polymer system, we employed AFM tapping mode analysis to assess the surface roughness of the prepared films using bar-coating film applicators, thereby evaluating its effect on the WCA. The AFM images qualitatively evaluated the topography of the surfaces of 1.5 wt% PDMS–PEG compared with those of bare PDMS in both AIR/PI and PI TOP/PI BOTTOM orientations (Fig. 3). Additionally, R_a (roughness average) and R_q (root mean square roughness) were determined based on all height variations (peaks and valleys) within 1 × 1 μm of composite surfaces. The AFM analysis revealed that the surface roughness of bare PDMS samples was significantly higher than that of PDMS:PDMS–PEG samples (Fig. S4). This observation indicates that while PDMS possesses a more hydrophobic surface, it also exhibits significantly rougher surface characteristics compared to PDMS:PDMS–PEG samples, making it less favorable for surface wetting. In contrast, the incorporation of PDMS–PEG appears to promote self-orientation of hydrophilic segments toward the surface during curing, contributing not only to enhanced surface wettability but also to smoother surface morphology. This behavior is consistent with Wenzel's model, where increased surface roughness amplifies the material's intrinsic wettability, leading to higher contact angles in hydrophobic PDMS and lower contact angles in smoother PEG-modified surfaces.[41] Furthermore, the surfaces interfaced with PI, both in bare PDMS and 1.5 wt% PDMS–PEG samples, demonstrated more uniform and homogeneous topography compared to those exposed to air. This observation highlights the important role of polymer–substrate interactions during curing in determining the final surface structure and its contribution to consistent wetting behavior.

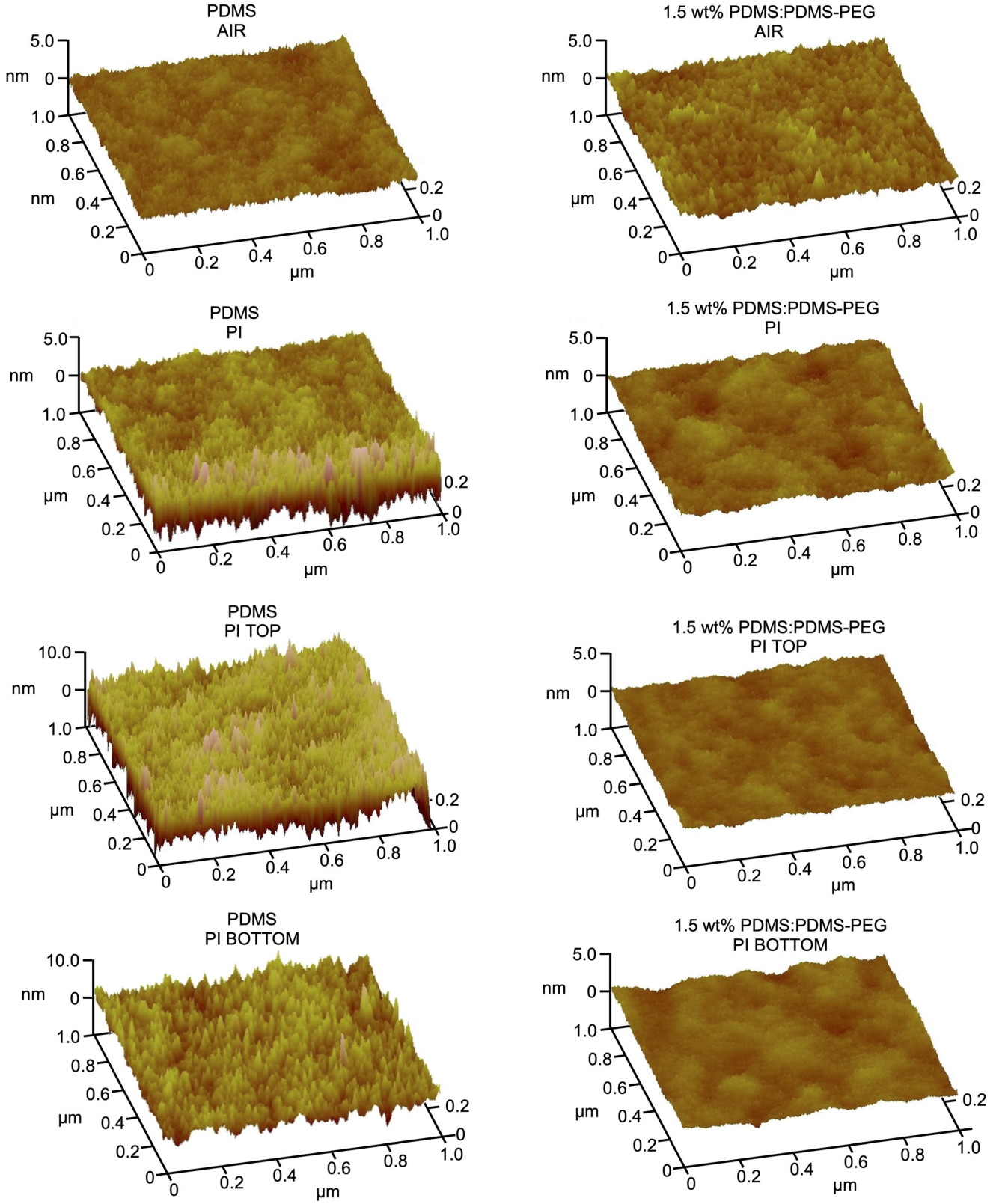

Fig. 3 Surface characterization of PDMS and PDMS:PDMS–PEG films using AFM (tapping mode). Atomic force microscopy (AFM) images of pristine PDMS and 1.5 wt% PDMS:PDMS–PEG films were obtained to analyze the surface morphology under two fabrication configurations: AIR/PI and PI TOP/PI BOT.

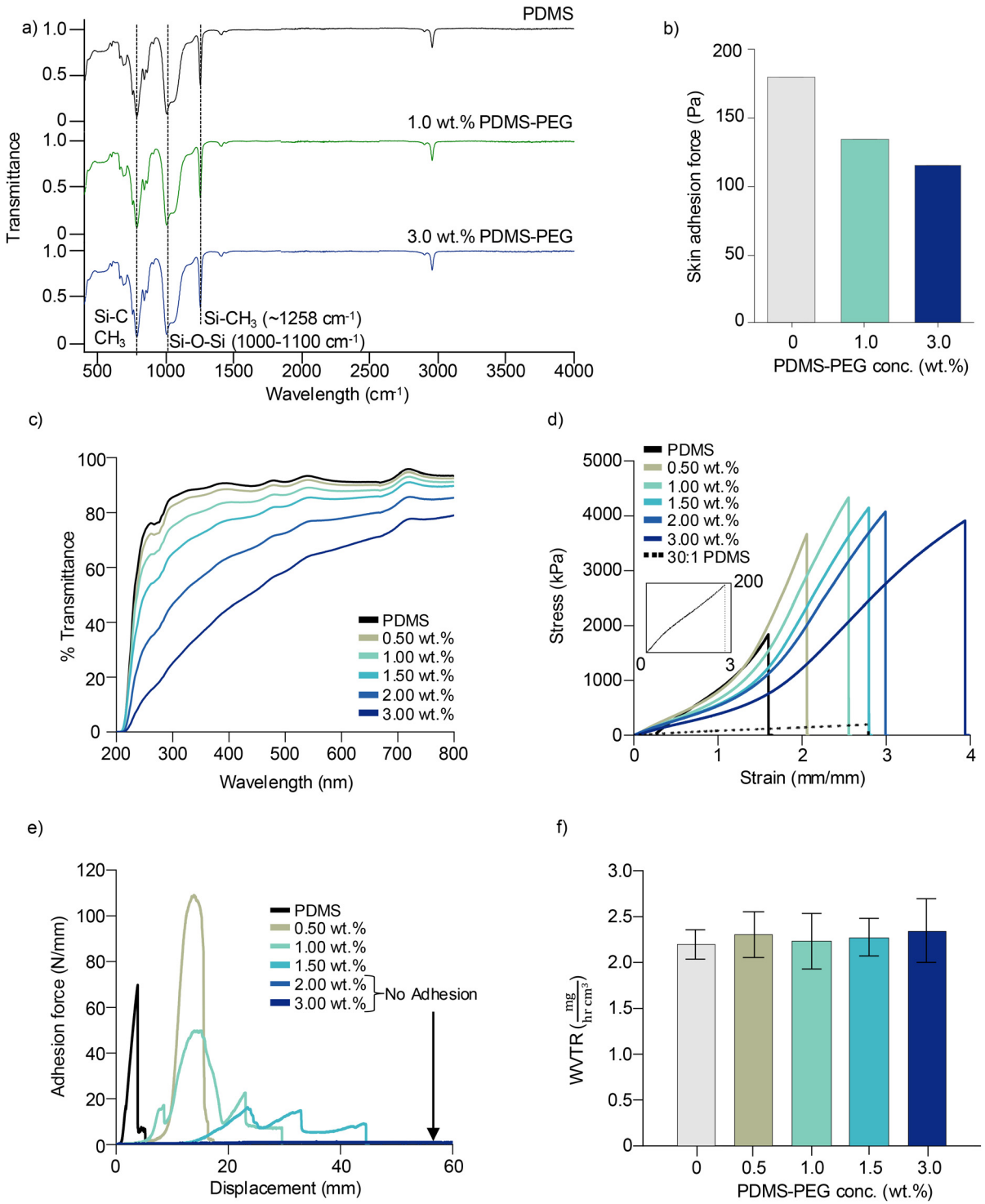

Fig. 4 Physical and mechanical characterization of PDMS:PDMS–PEG films with varying PEG contents. (a) Fourier-transform infrared spectroscopy (FT-IR) of PDMS:PDMS–PEG films containing 0, 1.0, and 3.0 wt% PDMS–PEG, confirming the chemical incorporation of the PDMS–PEG block-copolymer. (b) Wet skin adhesion force measurements containing 0, 1.0, and 3.0 wt% PDMS:PDMS–PEG films on the forearm. (c) UV-vis spectroscopy analysis of PDMS:PDMS–PEG films to evaluate optical transparency across different PEG wt%. (d) Tensile testing of PDMS:PDMS–PEG films to determine mechanical properties, including tensile strength and elongation. The inset figure shows the tensile strength and elongation of the 30 : 1 PDMS film. (e) Plasma bonding adhesion strength assessment using a free-standing T-peel test setup, comparing PDMS:PDMS–PEG films with different PEG wt% plasma bonding to pristine PDMS. A schematic diagram of the test configuration is included. (f) Water vapor transmission rate (WVTR) measurements of PDMS:PDMS–PEG films across various PEG wt% to evaluate barrier properties.

Physical and mechanical characterization of the PDMS: PDMS–PEG block copolymer composite

The assessment of PDMS:PDMS–PEG films focused on properties essential for the fabrication of skin-interfaced microfluidic sweat collection devices. The chemical composition of the fabricated films was characterized using Fourier-transform infrared spectroscopy (FTIR) to identify the incorporation of the PDMS–PEG block copolymer into the PDMS matrix. The full spectra were collected for films with 0, 1, and 3 wt% of the copolymer additive under AIR-PI and PI Top-PI Bot fabricated conditions (Fig. S5). The spectrum shown in Fig. 4a are the representative FTIR spectra for 0, 1, and 3 wt% PDMS:PDMS–PEG films. The spectrum of the PDMS film displayed characteristic transmission peaks, including the Si–O–Si asymmetric stretching from 1000–1100 cm^{-1}, the CH_3 symmetric bending peak (Si–CH_3) near 1258 cm^{-1} and Si–C stretching/CH_3 rocking bands in the 780–840 cm^{-1} region. Upon addition of the PDMS–PEG block copolymer, the spectra remained dominated by PDMS features, as expected given the copolymer's composition. However, specific changes were observed that indicated the presence of the PEG segments. A shoulder peak appeared around 2870 cm^{-1}, corresponding to the C–H stretching vibrations of ethylene groups in the PEG blocks (Fig. S5a). The Si–O–Si absorption band between 1000 and 1180 cm^{-1} broadened (Fig. S5a), which is consistent with an overlapping C–O–C ether stretching from the PEG chain. A comparison of samples fabricated under Air-PI and PI Top-PI Bot conditions (Fig. S5b) showed negligible spectral differences, suggesting that the bulk chemical composition was not significantly affected by the surface curing environment. Therefore, the FTIR analysis confirms the incorporation of the PDMS–PEG block copolymer into the PDMS matrix. Although this study did not evaluate the PDMS: PDMS–PEG material under prolonged aqueous immersion, the lack of covalent bonding to the Sylgard 184 PDMS network suggests that water exposure may cause PEG leaching and a gradual loss of surface hydrophilicity.

The skin adhesion properties of the films were characterized to assess their suitability for direct skin contact. A clear, concentration-dependent trend was observed, where the skin adhesion force decreased with an increasing weight percentage of the PDMS–PEG copolymer (Fig. 4b). The unmodified PDMS film (0 wt%) exhibited the highest adhesion force at approximately 180 Pa. Upon incorporation of the copolymer, the adhesion force was reduced to ~135 Pa for the 1 wt% film and further decreased to ~115 Pa for the 3 wt% film. This inverse relationship indicates that the PEG content can be used to effectively modulate the adhesive properties of the material, a key parameter for designing comfortable, skin-interfaced devices.

Some of the skin-interfaced microfluidic devices utilize onboard spectroscopic analysis, such as colorimetric[22] and fluorometric sensing[39] methods, for analyzing the concentration of sweat biomarkers. To assess the optical properties of the composite materials, we investigated the transmittance of the PDMS:PDMS–PEG films (~500 μm thick) with varying PEG wt% concentrations using UV-vis spectroscopy (200–800 nm) (Fig. 4c). The composite films with PEG concentrations up to 0.5 wt% demonstrated optical properties comparable to pure PDMS. However, higher PEG concentrations led to decreased transmittance and a notable loss of transparency. Meanwhile, higher concentrations of PDMS–PEG increased opacity, potentially impeding transmission-based optical measurements. However, carefully placing the resulting off-white background may improve the contrast and visibility of colorimetric assays. Consequently, the current scope of this paper does not include on-board colorimetric assays, so we have opted to use PDMS: PDMS–PEG for the channel layer and pure PDMS for the enclosing layer in our experiments involving human subjects in the subsequent sections.

In Fig. 4d, the stress–strain curves of the PDMS:PDMS–PEG films show that increasing the PDMS–PEG wt% enhances both the stretchability and plateau stress of the resulting composite. This plateau stress likely arises from the uncoiling of PEG segments within the polymeric network, which contributes to the improved elasticity of the composite structure. Even a small addition of 0.5 wt% PEG block copolymer to a 10 : 1 PDMS matrix resulted in increases of the elasticity and ultimate tensile strength by 28% and 99%, respectively. Further additions of PDMS–PEG BCP increase the yield strain of the composites. Further incorporation of PDMS–PEG BCP led to a progressive increase in yield strain, reaching approximately 74% at 2 wt%—a value comparable to that of a much softer 30 : 1 PDMS formulation. The elastic region steepened with increasing PDMS–PEG content, indicating an increase in the elastic modulus and thus a stiffer response. Concurrently, the plastic deformation region was reduced, with failure occurring shortly after yielding in composites with higher PEG concentrations. This indicates enhanced compliance and mechanical softness, making the composite better suited for interfacing with soft biological tissues such as skin, where mechanical mismatch must be minimized to prevent irritation and device detachment. Moreover, ultimate tensile strength increased twenty-fold with the incorporation of 2 wt% PDMS–PEG compared to pristine 10 : 1 PDMS, reflecting a dramatic improvement in load-bearing capacity and resistance to mechanical failure. This is essential for the longevity and reliability of stretchable devices, especially in wearable applications subjected to frequent mechanical deformation. Young's modulus showed a decreasing trend with increasing PDMS–PEG wt%, indicating that the materials became softer and more deformable. This tunable stiffness is advantageous for biomedical applications, as it enables the composite to more closely mimic the modulus of human skin (ranging from 10 to 500 kPa depending on the body location), ensuring better mechanical integration and comfort. Overall, these mechanical enhancements, including increased stretchability, higher tensile strength, and reduced stiffness, translate into highly suitable properties for patch-type 3D sweat-monitoring devices. These materials offer the

flexibility and durability needed to withstand skin movements while maintaining conformal contact, ensuring consistent data collection and user comfort during long-term use.

Microfluidic devices must possess sufficient bonding strength to maintain integrity under mechanical stress caused by natural skin movement and internal pressure from sweat gland secretion. To evaluate interfacial bonding, composite films with varying PEG wt% were bonded to PDMS substrates using oxygen plasma treatment, and bonding strength was assessed *via* free-standing T-peel testing (Fig. 4e). The force-displacement curve indicated that the bonding efficiency significantly decreased at PDMS–PEG concentrations exceeding 1.5 wt% in the composite. This decline may be due to PEG segment saturation on the PDMS composite surface, which reduces the available surface functional groups for salinization. Also, the surface energy mismatch between PDMS–PEG and PDMS and the inability of plasma activation to adequately address PEG's chemical properties. Typically, oxygen plasma bonding creates strong bonds through surface activation, which facilitates robust and leak-free adhesion through the formation of covalent siloxane bonds. While plasma bonding is particularly effective for joining PDMS to PDMS interfaces, the presence of PEG functional groups appears to disrupt the bonding process, resulting in significantly reduced bond strength. To overcome the limitations of plasma bonding for PDMS:PDMS–PEG microchannels, we also employed a semi-cured bonding technique. This method involves the partial curing of the PDMS cover layer, which creates an adhesive surface that can bond with a fully cured PDMS–PEG channel layer. Unlike plasma bonding, this approach takes advantage of the inherent tackiness of uncured PDMS chains, allowing them to interpenetrate and crosslink with the pre-cured PDMS layer during thermal curing. We optimized process parameters for curing time and temperature. We evaluated the effectiveness of the semi-cured bonding technique through T-peel testing (Fig. S6), comparing the bond strength of PDMS–PEG layers joined using both plasma bonding and semi-cured bonding techniques. While the semi-cured method did not yield a statistically significant increase in bond strength, it consistently exhibited sufficient adhesion, even at the higher PDMS–PEG weight percentages, creating a bond robust enough to withstand physiological conditions such as active sweating and remained intact under applied fluidic pressures. The observed improvement in bonding performance is likely due to enhanced molecular interdigitation at the semi-cured interface, which bypasses the limitations of plasma activation. Achieving robust bond strength in skin-interfaced microfluidic devices highlights their reliability and functionality, particularly in applications involving fluid manipulation and long-term use and resilience in dynamic environments. The semi-cured bonding technique demonstrates a viable pathway for simple and straightforward hydrophilic modifications into PDMS-based devices without sacrificing structural integrity. This method not only expands the application of PDMS–PEG in biomedical microfluidics but also simplifies fabrication by eliminating the need for plasma activation equipment. The impressive mechanical properties—characterized by exceptional stretchability and strong interfacial bonding—demonstrate the device's excellent suitability for on-skin applications. Successful on-body trials, during which the devices remained intact in dynamic areas of the body, provide compelling qualitative evidence of the channel's remarkable stability during bending and natural movement. A systematic, long-term mechanical evaluation of the fully assembled device will further enhance our understanding of how to develop such systems for commercial applications.

The evaporation of liquids in microfluidic devices is a concern for the long-term measurement of samples stored in the device, whether for on-board or offline measurements. We determined the water vapor transmission rates (WVTRs) for PDMS:PDMS–PEG films using the permeability cup method based on ASTM standard F1249. The WVTR results shown in Fig. 4f indicate that the addition of the PDMS–PEG block copolymer did not statistically significantly alter the WVTR of the resulting film. Although the hydrophilicity of the composite improved with the incorporation of the PDMS–PEG block copolymer, water vapor transmission remained similar to that of pure PDMS. While the current WVTR characteristics are sufficient for short-term measurements, further optimization will be necessary to minimize sample evaporation in soft epidermal microfluidic systems, and this remains an area of ongoing investigation.

In vitro microfluidic characterization of PDMS–PEG

The mechanism underlying sweat collection in skin-interfaced microfluidics is fundamentally based on capillary action and active transport facilitated by the pressure of sweat glands. However, the inherent hydrophobicity of PDMS introduces a threshold pressure that must be surpassed to overcome the resistance against fluid flow at the inlet. The enhancement in hydrophilicity is expected to reduce the threshold pressure for fluid entry, which may facilitate accurate and effective fluid transport for storage and analysis. The experimental setup for measuring the threshold pressure and advancing contact angle of PDMS and PDMS–PEG films is depicted in Fig. 5a and Video S1. A constant pressurized flow of liquid using a microfluidic pressure-based flow control (Flow EZ™, Fluigent) within plastic tubing was directed onto the printed stage, wetting the space between the medical adhesive and eventually entering inlet channel (dia. 0.9 mm). This system recreates the interface of the skin, medical adhesive, and inlet features of soft hydrophilic microfluidics. The pressure for this continuous flow gradually increased by 10 Pa per minute to ensure precision while measuring the advancing contact angle.

The threshold pressure measurements in Fig. 5b were demonstrated to be the highest with the native PDMS fluidic system but decreased by 40% with the incorporation of 0.5 wt% PDMS–PEG BCP. Increasing the PDMS–PEG BCP content further led to a continued reduction in the threshold pressure, though the change became negligible beyond 1.5

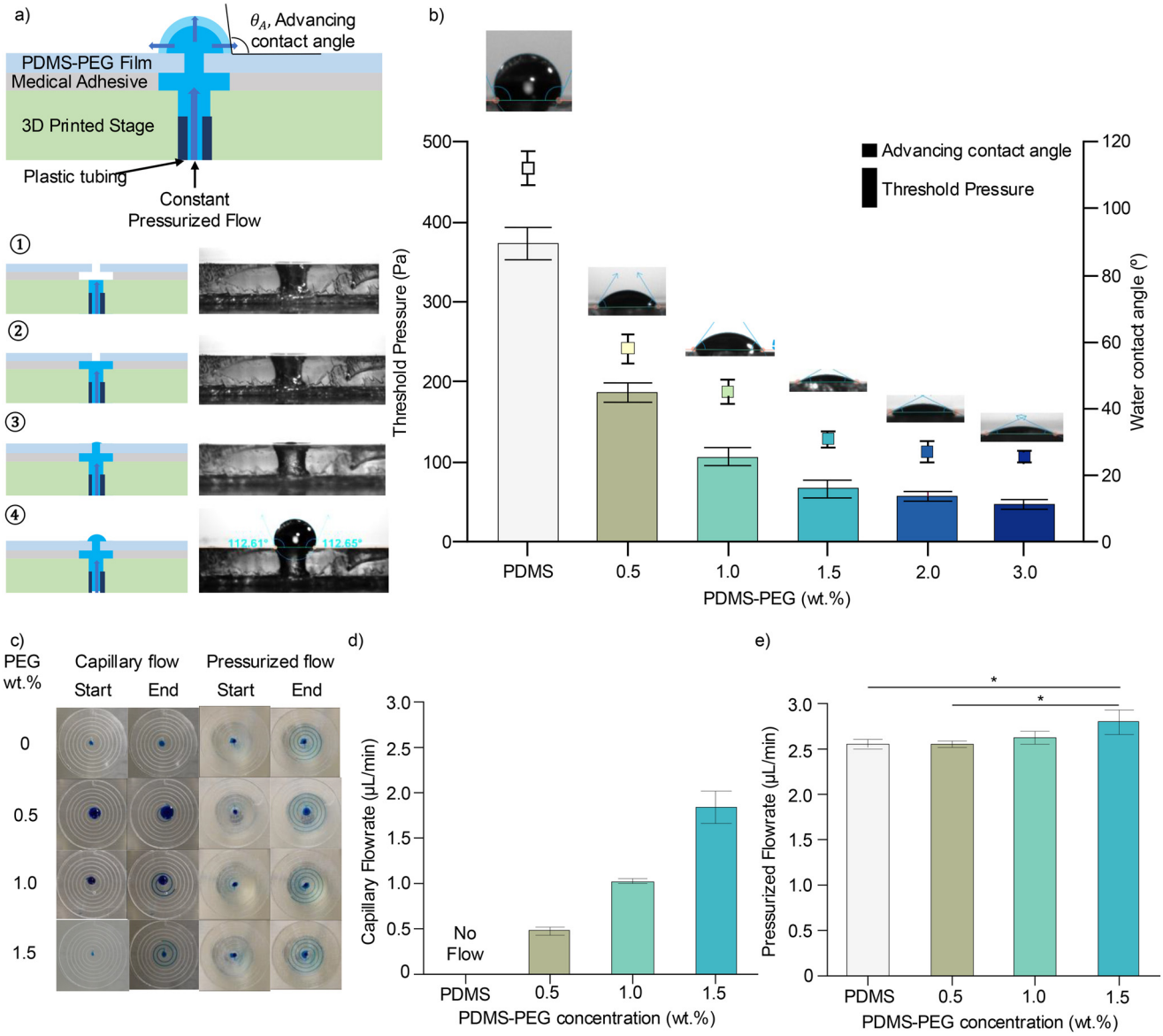

Fig. 5 *In vitro* microfluidic assessment of PDMS:PDMS–PEG devices. (a) Schematic illustration of the threshold pressure measurement setup using a 20-gauge needle-punched inlet, along with the method for advancing contact angle measurement. (b) Quantitative analysis of the threshold pressure (bars, left axis) and advancing contact angle (points, right axis) as a function of PDMS–PEG wt% concentration. (c) Representative images of microfluidic flow variations in PDMS:PDMS–PEG devices after 1 minute, demonstrating natural wetting capillary flow (left panels) and pressure driven flow (right panels). (d) Calculated capillary flow rates based on observed flow dynamics. (e) Microfluidic flow rate measurements under constant pressurized flow at 1 kPa. Statistical analysis was performed using the Games–Howell *post hoc* test ($n = 3$, $p < 0.05$).

wt% PDMS–PEG. With 1.5 wt% PDMS–PEG microfluidics, the threshold pressure dropped to approximately 70 Pa to collect an aqueous sample, a value significantly lower than the natural sweat production of ~2 kPa. A similar trend was observed in the advancing contact angle. The PDMS fluidics exhibit the highest value at around 110° of advancing WCA, which significantly dropped to 58° at 0.5 wt% PDMS–PEG. Continued hydrophilic block copolymer addition further lowered the advancing contact angle, reaching approximately 30° at 1.5 wt% PDMS–PEG. Although plasma bonding of PDMS–PEG films, which is necessary for 3D microchannel fabrication, became infeasible beyond this concentration, the semi-cure bonding methods enabled us to test sweat harvesting with a 1.5 wt% PDMS–PEG system. These results highlight that PDMS–PEG BCP incorporation substantially enhances external-pressure aided hydrodynamic flow within the microchannel, compared to unmodified PDMS devices.

To quantitatively assess the impact of hydrophilic modification on capillary-driven flow, we applied Jurin's Law to estimate the theoretical capillary rise for various PDMS–PEG BCP concentrations. Contact angle values were used to calculate capillary height using the following parameters: a sweat surface tension (γ) of 0.0728 N m^{-1}, a density (ρ) of 1 g cm^{-3}, a gravitational acceleration (g) of

9.81 m s^{-2}, and a capillary radius (r) of 0.455 mm. Measured contact angles (θ) were 110° for unmodified PDMS, 58° for 0.5 wt% PDMS–PEG, and 20° for 1.5 wt% PDMS–PEG. As shown in SI Table S2, the results indicate a 2.77-fold increase in capillary rise from native PDMS to PDMS–PEG (1.5 wt%), underscoring a substantial enhancement in spontaneous fluid transport resulting from hydrophilic surface modification. The negative capillary height in PDMS reflects its inherent hydrophobicity, which resists passive fluid transport. In contrast, the PEG-modified surface facilitates efficient, passive sweat uptake into microchannels independent of external driving force (*i.e.*, sweat pressure). This enhanced capillary behavior observed in PDMS–PEG is primarily attributed to a reduction in advanced contact angle, which increases wettability and lowers the pressure threshold for fluid entry. Efficient capture of initial "primer" sweat is especially critical for metabolomic analysis, as it contains the highest concentration of biomarkers. In general, primer sweat that cannot overcome the inlet threshold pressure is often reabsorbed into the skin surface, leading to unreliable and inaccurate analytical measurements. By promoting rapid and passive uptake of this early fluid phase, PDMS–PEG devices improve sampling fidelity, increase biomarker yield, and ultimately enable more accurate and reliable data acquisition in wearable diagnostic platforms.

A simple spiral microfluidic device was designed, inspired by a standard, commercially available sweat collection device (*i.e.*, Macroduct®), and fabricated using a 3D-printed mold and standard soft lithography techniques. As shown in the representative images in Fig. 5c, natural capillary flow was assessed in PDMS and PDMS–PEG devices by placing a single water droplet (~187 Pa) at the microfluidic device entrance (Video S2). The calculated capillary flow rates are plotted in Fig. 5d. As expected, the unmodified PDMS device exhibited no observable capillary-driven flow. In contrast, incorporation of 0.5 wt% PDMS–PEG enabled a spontaneous flow rate of ~0.48 μL min^{-1}, which increased over 3.8-fold to ~1.86 μL min^{-1} at 1.5 wt% PDMS–PEG. This enhancement in capillary flow is attributed to the increased channel wettability, as confirmed by advanced contact angle measurements. The ability to sustain passive liquid transport in PDMS–PEG devices is particularly beneficial for continuous sweat sampling, especially under low-sweat conditions such as those encountered in clinical or sedentary environments. This enhancement in spontaneous, capillary-driven flow is a key advantage of our hydrophilic material, directly addressing the significant challenge of collecting sweat at the low flow rates typical of sedentary or resting conditions. This challenge has been the focus of recent innovative device-level designs. For example, the work by Saha *et al.* has demonstrated platforms that use zero-power osmotic sweat extraction for the continuous monitoring of analytes like lactate[29] and glucose[30] at rest, while Nyein *et al.* have developed patches with hydrophilic fillers for rapid sweat uptake and to combat evaporation.[31] Our work contributes a complementary, material-centric solution to this problem. By engineering the intrinsic hydrophilicity of the microfluidic channel itself, we enable passive, spontaneous sweat transport, providing a foundational material improvement that can enhance these sophisticated device architectures.

To further evaluate performance under physiologically relevant conditions, we measured *in vitro* flow rates while applying a constant pressure of 1 kPa, which is within the range of human sweat gland pressure (Video S3). As shown in Fig. 5e, devices with higher PEG concentrations exhibited increased flow rates. The flow rate modestly but significantly increased from ~2.56 μL min^{-1} in the native PDMS device to ~2.88 μL min^{-1} in the 1.5 wt% PDMS–PEG device. The differences between the native PDMS device and both the 1.0 wt% and 1.5 wt% devices were statistically significant ($p < 0.05$). The pressurized flow demonstrated greater stability and less variability than the capillary-driven flow. Under external pressure, fluid transport is dominated by forced convection, leading to a consistent flowrate. In contrast, capillary-driven flow relies on surface tension forces at the advancing meniscus, making it more susceptible to microscopic variations in channel wettability. Nonetheless, the significantly elevated flow rate observed in the 1.5 wt% PDMS–PEG device supports its capacity for improved fluid transport, enhancing the utility of the device in low-pressure, sweat-driven environments.

Pilot feasibility human study: non-physical *vs.* physical exercise activity

A pilot feasibility study was conducted to evaluate the on-body performance of sweat harvesting using 1.5 wt% PDMS–PEG microfluidic devices against unmodified PDMS devices. In a non-exercise trial, devices were worn on the forearm of a human subject for half a day in an environment that included both air-conditioning (AC) and non-air-conditioning (Fig. 6a). Initially, under ambient indoor conditions with AC, no sweat was collected in either device, likely due to suppressed sweat gland activity in the absence of thermal, pharmaceutical, or physical stimulation.

Sweat collection initiated only after periods of increased thermal load—specifically, after moving outdoors and during non-air-conditioned mealtimes, which are known to induce gustatory and postprandial sweating. As shown in Fig. 6a, the PDMS–PEG device demonstrated superior collection efficiency, capturing nearly double the sweat volume compared to the unmodified PDMS device during these active sweating periods. The inset in Fig. 6a further highlights that the modified device exhibited a steeper slope of fluid accumulation, indicating a higher volumetric flow rate. This confirms that the enhanced hydrophilicity of the PDMS–PEG material translates to more efficient fluid uptake on-body. However, it was also observed that the collected fluid in the PDMS–PEG channels evaporated more rapidly during periods of no sweat production, likely due to the larger wetted surface area exposed to air. Crucially, the mode of evaporation provides a significant operational advantage for the hydrophilic device. As observed during the trial, the liquid in the hydrophobic PDMS device tends to break apart into discrete droplets upon evaporation (Fig. S7). These

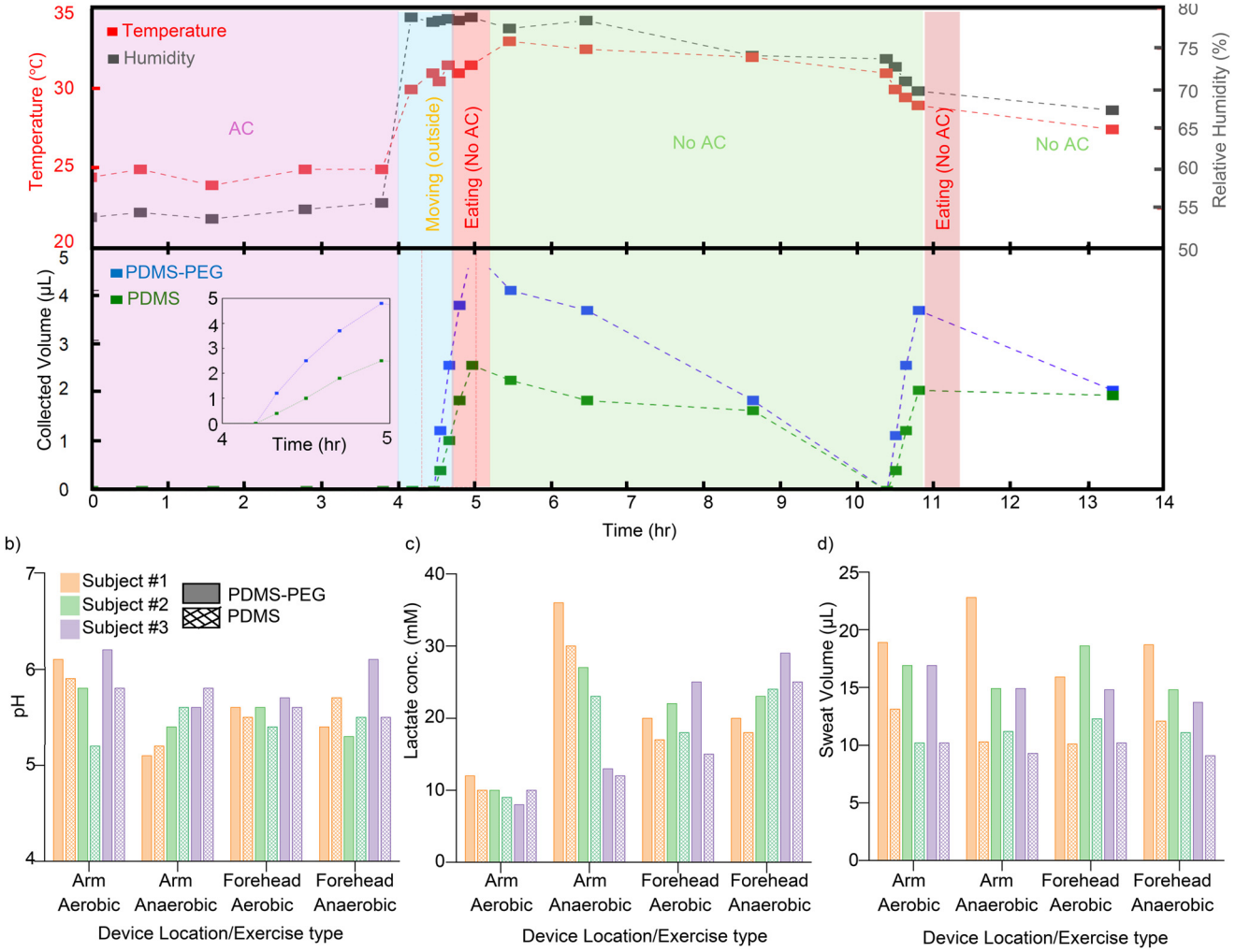

Fig. 6 Feasibility study of the PDMS:PDMS–PEG microfluidic devices in human subjects. (a) Images from a half-day, non-exercise wear test showing the PDMS:PDMS–PEG and PDMS microfluidic devices applied to the forearm before and after sweat collection. (b–d) Results from an exercise-based study evaluating: (b) sweat pH, (c) lactate concentration, and (d) sweat volume collected using the PDMS:PDMS–PEG and PDMS devices.

isolated liquid pockets can create a high-pressure barrier, effectively forming a barrier that prevents new sweat from flowing through the channel and can render the device inoperable. In contrast, the liquid in our hydrophilic PDMS–PEG device recedes as a continuous, unbroken line, maintaining an open pathway and ensuring the device remains functional for subsequent sweat collection. While mitigating the overall evaporation rate is an important goal for future work, this mechanism for preventing channel blockage is a key advantage for reliable, long-term operation.

To further assess the device's utility for biomarker analysis, an exercise-based study was performed with three human subjects (Fig. 6b–d). The pH and lactate concentrations of the collected sweat were analyzed post-collection. Fig. 6b and c show that there were no significant differences in pH levels between the samples collected from the PDMS and PDMS–PEG devices under any of the exercise conditions. However, it is important to note that lactate concentrations tended to be slightly elevated in the PDMS–PEG devices. This suggests that the PDMS–PEG material does not chemically alter these specific biomarkers. While quantitative intensity metrics such as heart rate were not recorded in this pilot study, the "aerobic" and "anaerobic" sessions were designed to produce distinct modes of respiration during physical exertion of the human study subjects, and the results align with expected physiological responses. Notably, lactate concentrations were consistently higher during anaerobic arm exercises compared to aerobic exercises across all subjects, which aligns with expected physiological responses to different exercise intensities. While lactate was consistently elevated during anaerobic arm exercises, the effect was less pronounced on the forehead. This is likely because sweat lactate reflects local glandular metabolism rather than systemic levels, and the anaerobic exercises engaged arm musculature more intensely than facial muscles.

Critically, the PDMS–PEG devices consistently collected a larger sweat volume than the standard PDMS devices across all subjects and exercise conditions (Fig. 6d). The PDMS–PEG devices collected approximately 58% more sweat than PDMS devices across all exercise conditions and body locations.

This enhanced collection volume is a direct result of the device's improved hydrophilicity and the reduced threshold pressure required for fluid entry, which allows for more efficient capture of sweat from the glands. The ability to collect larger sample volumes is a significant practical advantage, as it ensures sufficient volume for analysis with standard laboratory instruments like LC-MS. While this study did not involve real-time sensing, the observed higher flow rates and dynamic fluid movement in the PDMS–PEG devices are highly relevant for future applications in electrochemical sensing, where such factors directly influence the temporal resolution and accuracy of real-time analyte measurements.

Accurate metabolomics of sweat requires collecting a defined volume rapidly into a sealed, low-adsorption path to minimize evaporation, contamination from skin/cosmetics, and loss of labile metabolites. Our hydrophilic PEG–PDMS microchannels meet these requirements at low secretion rates, allowing for concentration-calibrated and time-resolved sampling without post-treatment. The hydrophilic sweat collection device demonstrates how this composite material innovation can advance sweat analysis beyond conventional methods. Given that the full clinical relevance of the sweat metabolome remains under investigation, capturing a high-fidelity sample is crucial for expanding our fundamental understanding of its composition. The following analysis of sweat from human subjects (Fig. 7), therefore, utilizes our hydrophilic platform to provide a comprehensive snapshot of key metabolites and highlight the advantages of this collection strategy. Participants wore two PDMS microfluidic devices and two 1.5 wt% PDMS–PEG microfluidic devices, each with a capacity of 50 μL, on their lower back while engaging in low-impact aerobic activity. The exercise consisted of 40 minutes of treadmill walking at 3 mph with a 3% incline. Sweat collected during the workout was analyzed for common biomarkers and inflammatory markers using high-resolution instrumentation, including trapped ion mobility spectrometry (TIMS) as an orthogonal separation technique alongside conventional high-performance liquid chromatography (HPLC) and time-of-flight (TOF) mass spectrometry (MS). This increase in sweat volume collection is significant as it can lead to improved data quality, facilitate downstream sample preparation for precision biomarker analysis, and enhance the resolution of hydration profiling—capabilities that are often limited in PDMS-only systems. In both spectroscopic and TIMS TOF MS analysis, there were significant differences in sweat metabolite concentration observed between the PDMS–PEG and PDMS devices. While the composite material does not chemically alter biomarkers, the concentrations of biomarkers collected using the PDMS–PEG device were generally higher than those gathered with the PDMS devices. This difference may be attributed to improved primary sweat collection techniques and lower sweat rates. This accumulation over the entire sweat secretion phase likely averages out transient changes in biomarker concentration. This improvement is attributed to enhanced channel wettability and lower resistance to flow despite comparable physiological sweat pressure. Collecting larger volumes is particularly advantageous for individuals with low sweat rates and supports improved detection sensitivity for laboratory-based assays. Although the real-time electrochemical analysis was not employed in this study, the observed increase in dynamic fluid flow and meniscus movement suggests that PDMS–PEG microfluidics may significantly enhance temporal resolution and analyte stability in future real-time sweat-sensing platforms, exciting possibilities for future research.

Sweat samples were obtained from four individual subjects using direct sampling (*i.e.*, SCOOP), a standard PDMS microfluidic device, and a 1.5 wt% PDMS–PEG device. The collected samples were then analyzed to quantify key metabolites and evaluate differences attributable to the sampling method. Sample preparation involved centrifugation followed by dilution with LC-MS grade water to enable higher injection volumes. The prepared samples were loaded into LC-MS-compatible cartridges, with injection volumes set to 10 μL.

The resulting LC-MS data were rigorously preprocessed to ensure analytical integrity, including noise filtering, artifact removal, and exclusion of background signals identified in blank controls. Peak picking, alignment, and normalization were performed prior to qualitative analysis to ensure robust and reproducible biomarker comparisons across sweat collection methods. Heatmaps of the top 100 biomarkers in both positive ($[M + H]^+$) and negative ($[M - H]^-$) ion modes revealed that PDMS–PEG devices consistently captured the higher signal intensities for a broad range of metabolites compared to the other methods (Fig. 7d and e). This enrichment is attributed to hydrophilic microchannel surfaces, which promote rapid harvest of 'primer sweat'—the earliest, most concentrated fraction of sweat rich in analytes. It is well-established that biomarker concentrations are often inversely correlated with sweat rate due to a dilution effect. Our device directly mitigates this confounding factor by efficiently capturing sweat at its initial, low-secretion phase before significant dilution can occur. In contrast, hydrophobic PDMS devices delay fluid entry, preferentially sampling sweat from higher, more diluted flow rates and allowing the initial primer sweat to be lost. The SCOOP method, collected post-exercise, likely missed this critical phase entirely or inaccurately represents it due to sweat evaporation. These findings highlight the importance of capturing primer sweat for accurate, clinically reliable, high yield metabolomic profiling. For instance, trans-epidermal water loss and rapid evaporation at the skin surface can significantly reduce analyte availability when passive or delayed collection strategies are used.[42] The PDMS–PEG devices mitigate this loss by enabling immediate uptake and preserving labile biomarkers, enhancing both sensitivity and data fidelity in wearable sensing applications.

For quantitative analysis, we focused on hydrocortisone, L-lactate, and L-tryptophan due to their growing relevance in clinical and wearable diagnostics for stress monitoring, occupational health, and overall quality-of-life assessment.

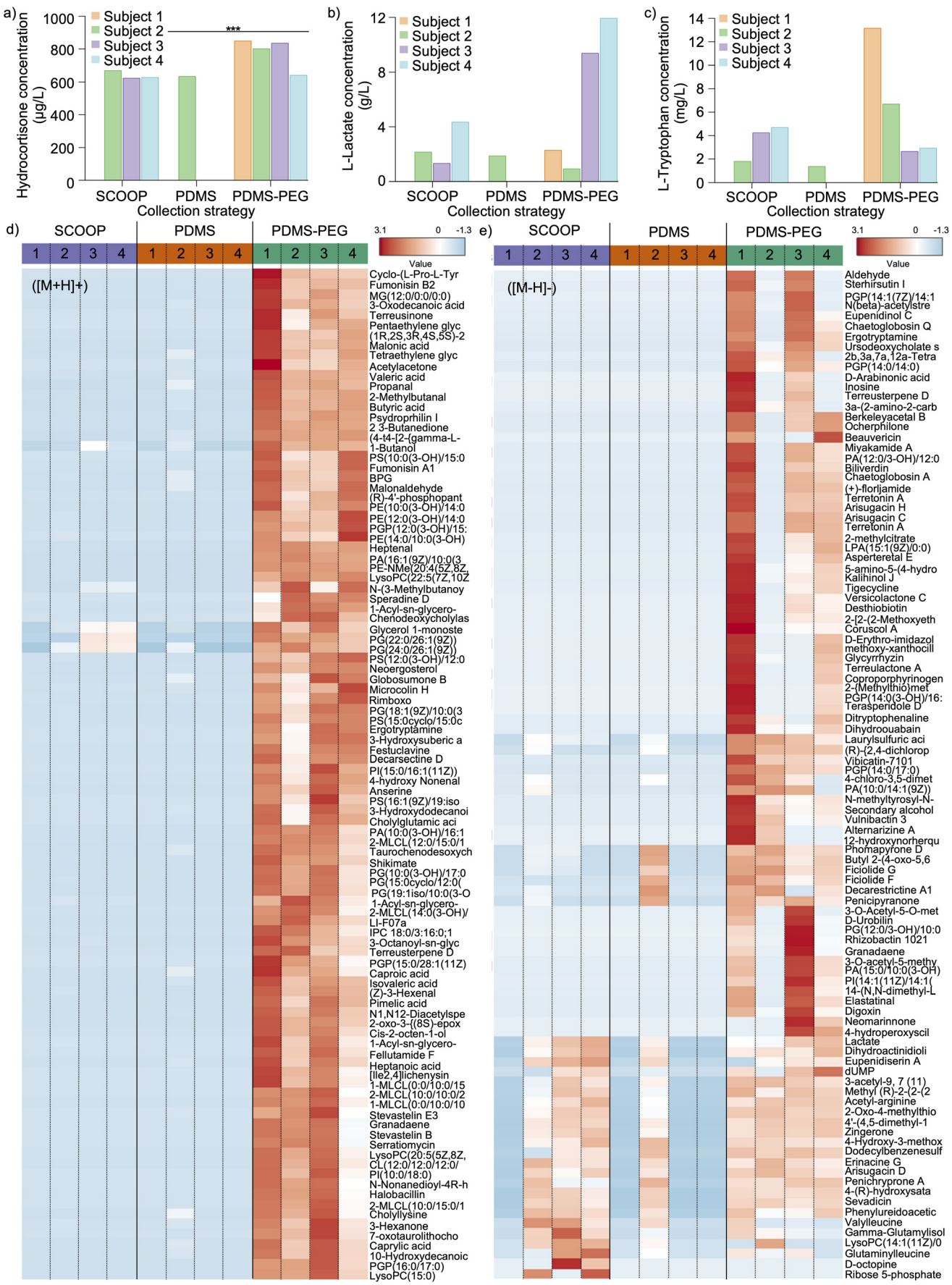

Fig. 7 LC-MS metabolomics analysis of sweat samples collected using different strategies. Standard curves were used to quantify the concentrations of: (a) hydrocortisone, (b) L-lactate, and (c) L-tryptophan across human subjects for each collection method. (d) Positive ion mode and (e) negative ion mode analysis heatmaps showing the top 100 most significant biomarkers identified for each collection strategy.

Hydrocortisone (cortisol) serves as a key biomarker for stress and circadian rhythm regulation, L-lactate reflects local metabolic activity and anaerobic respiration, and L-tryptophan is a precursor to serotonin and melatonin, often linked to mental health and neuroendocrine function. In biological fluids like sweat, cortisone remains neutral, exhibiting low overall polarity due to its largely nonpolar steroid structure. Lactate, present as the negatively charged lactate ion (COO^-) at physiological pH, is highly polar and hydrophilic, facilitating its efficient transport in sweat. L-Tryptophan exists as a zwitterion (with both NH_3^+ and COO^- groups), giving it moderate polarity; this allows it to interact with both hydrophilic and hydrophobic components in sweat, although its relatively bulky and aromatic side chain reduces its overall solubility compared to small polar metabolites like lactate. While PDMS is known to interact with small hydrophobic molecules and potentially interfere with LC-MS signals, these effects were considered negligible in our analysis for targeted biomarkers due to the strength of the analytical signals and the comparative nature of the study.

TIMS TOF LC-MS analysis demonstrated that sweat collected using the PDMS–PEG devices consistently contained higher concentrations of all three biomarkers compared to both standard PDMS and SCOOP collection methods. This improvement is likely driven by the enhanced hydrophilic properties of PDMS–PEG, which facilitate more effective initial sweat capture and sustained fluid uptake, resulting in increased sample volumes. Greater sample volumes contribute to reduced analytical variability and improved detection sensitivity, allowing for more precise quantification of physiological biomarkers. These results indicate that PDMS–PEG materials offer a technical advantage for sweat-based analysis, capturing more representative and reliable sweat profiles, making them a superior platform for noninvasive biomonitoring.

As shown in Fig. 7a, hydrocortisone concentrations have been determined to be over 1100 μg L^{-1} in the PDMS–PEG samples—substantially higher than the ~800–900 μg L^{-1} observed in PDMS and SCOOP methods, and far exceeding the typical physiological range of ~0.43 to 50.2 μg L^{-1} reported using immunoassays or electrochemical analysis with soft skin-interfaced microfluidics. This discrepancy likely reflects improved sampling of glandular secretion and reduced dilution due to earlier capture, as well as diurnal influences, as most samples were collected in the morning, when cortisol levels are typically the highest.

L-Lactate concentrations in the PDMS–PEG samples exceeded 1.2×10^7 μg L^{-1} in some subjects, compared to $<5 \times 10^6$ μg L^{-1} with PDMS and SCOOP (Fig. 7b). Sweat lactate arises largely from local eccrine gland metabolism and glycogen breakdown, rather than blood plasma levels, often resulting in higher concentrations under conditions of exertion or thermal stress. Factors such as muscle mass and metabolic activity in various geometric areas also contribute to interindividual variability. The subjects partaking in the physical activity study with lower muscle mass percentages correlated to higher concentrations of lactate. Subject 3 and subject 4 had the lowest muscle masses but the highest lactate concentrations, especially in the samples collected using PDMS–PEG. Systematic investigations are currently being conducted to explore the various factors, such as muscle mass, that influence sweat lactate concentration in comparison to overall serum lactate levels in the body.

Similarly, L-tryptophan levels peaked at 14 000 μg L^{-1} in the PDMS–PEG devices, compared to less than 6000 μg L^{-1} using other sampling methods (Fig. 7c). Although tryptophan is not routinely quantified in sweat, these markedly elevated concentrations suggest that the PDMS:PDMS–PEG platform offers enhanced analyte recovery. Additionally, the observed differences may reflect meaningful biological variation, potentially tied to individual metabolic or physiological states. These findings highlight the importance of the sampling method in accurately capturing sweat metabolite profiles. The superior performance of the PDMS:PDMS–PEG devices shows their potential for high-sensitivity biomarker detection, which is critical for applications in personalized health monitoring and noninvasive diagnostics. Optimizing the sampling method can dramatically influence metabolite detection, and the PDMS:PDMS–PEG approach shows strong promise for capturing low-abundance or previously underreported analytes in sweat. Recent work has demonstrated the feasibility of sweat-based tryptophan sensing using a molecularly imprinted, anti-fouling hydrogel sensor to selectively detect tryptophan in sweat.[43]

To explore protein-level differences across sweat collection methods, samples from the SCOOP and PDMS–PEG devices were analyzed from two individual subjects. Proteomic profiling identified over 9000 proteins, with 1366 high-confidence proteins retained following stringent filtering ($Q < 0.05$) and contaminant removal (Table S4). These proteins were consistently detected across all samples, enabling robust comparative analysis. Principal component analysis (PCA) revealed partial separation by the collection method, with SCOOP samples clustering together —suggesting that the sampling approach can influence the proteomic landscape. While biological replicates contributed to some variability, the observed clustering supports a potential method-dependent bias in protein recovery. Interestingly, differential expression analysis, adjusted for false discovery rate (FDR), did not yield statistically significant proteins (adjusted $p < 0.05$). However, ranking proteins by absolute $\log_2$ fold-change revealed several candidates with meaningful differences in abundance. Notably, ADP-sugar pyrophosphatase and immunoglobulin heavy constant gamma 1 (IgG1) were elevated in the SCOOP samples; these proteins are commonly found in human skin tissues and may be secreted into sweat or could be introduced as contaminants from the epidermis during the sampling process. This observation supports the hypothesis that direct scooping from the skin may introduce additional contaminants or exogenous proteins, including those from

skin contact or topical products. In fact, some detected markers, such as calmodulin-like protein 5 and triosephosphate isomerase, may be associated with dermal layers or reflect residual material from personal care products (*e.g.*, moisturizers, sunscreens, or cosmetics). This suggests that the SCOOP method could lead to overrepresentation of non-sweat-derived proteins, thereby confounding the true biological signals. These findings emphasize the importance of minimizing skin contact during sweat sampling to reduce contamination and improve the specificity of proteomic analyses. In this preliminary study, we propose that enzymes and structural proteins found in sweat can provide valuable insights into active cellular metabolism and turnover. Additionally, the presence of IgG1 and galectin-3 suggests that sweat may be an active component of the skin's immune defense system and could serve as a clinically relevant biomarker. The identified proteins may still hold value as potential biomarkers, but further validation in larger, well-controlled cohorts is needed to disentangle true physiological signals from sampling artifacts.

These metabolomics and proteomics analyses reveal the analytical advantages of the PDMS–PEG microfluidic devices in capturing sweat biomarkers with enhanced fidelity and sensitivity, thus improving clinical and physiological relevance. The improved wettability and fluid dynamics of PEG-modified channels facilitate efficient uptake of early-phase sweat, which is critical for high-resolution biomarker profiling. These devices also show promise for multiplexed detection of small molecules and proteins, enabling more comprehensive sweat analysis in real-time or longitudinal formats. Continued optimization of material properties and channel design will be essential to preserve labile analytes and minimize evaporative loss—key requirements for advancing wearable biosensing technologies. As personalized health monitoring and metabolomics-driven diagnostics gain momentum, PDMS–PEG platforms represent a powerful and scalable tool for next-generation sweat-based diagnostics for clinical applications.

Conclusion

This study provides a comprehensive examination of the material and functional performance of PEG-modified PDMS for skin-interfaced microfluidic sweat diagnostics. By incorporating PEG block copolymers into PDMS using a single-step, straightforward composite preparation method, we achieved a significant and adjustable reduction in the surface tension of the microchannels. Additionally, the systematic studies examined the effects of interfacing materials in polymeric composites during the curing process. Our studies indicated that an optimal concentration of 1.5 wt% PEG effectively increased hydrophilicity without compromising the integrity of the device. Beyond this concentration, further enhancements plateaued, suggesting that the surface becomes saturated with PEG segments.

The PDMS–PEG microfluidic devices demonstrated superior capillary-driven flow and fluid transport capabilities compared to native PDMS, driven by reduced contact angles and enhanced interfacial properties. These advantages translated into markedly improved sweat collection performance during pilot human studies, with increased the uptake of early-phase "primer" sweat and higher sample volumes under both passive and active sweating conditions. Quantitative TIMS TOF LCMS metabolic analyses confirmed elevated concentrations of physiologically relevant biomarkers—including hydrocortisone, L-lactate, and L-tryptophan—highlighting the impact of improved material design on analytical sensitivity. Proteomic profiling further revealed that the collection strategy can influence protein recovery, underscoring the importance of device composition in preserving labile, low-abundance biomarkers such as cytokines and immunoglobulins.

Collectively, these findings establish PDMS–PEG as a highly versatile and analytically robust material platform for wearable sweat diagnostics. The current platform may be well-suited for niche applications that are challenging for conventional sweat sensors, such as biomarker monitoring in sedentary individuals for occupational, geriatric, or pediatric care. More importantly, it serves as an advanced tool for clinical research. Given that the full clinical relevance of the sweat metabolome is still under investigation, obtaining high-fidelity samples for laboratory-based analysis is vital for the foundational studies required to discover new biomarkers and better understand the link between sweat composition and systemic health.

While the current work relies on this laboratory-based analysis for validation, the reliable sample collection demonstrated here also provides the essential foundation for the next-generation of fully-integrated wearable sensors. Future work should therefore focus on integrating on-board electrochemical or colorimetric sensors to create an autonomous system for real-time analysis. Additionally, efforts must continue on developing evaporation mitigation strategies and assessing the long-term stability and scalability of these devices to fully realize their potential in continuous, noninvasive, and clinically meaningful health monitoring systems.

Our on-body studies have demonstrated the device's overall robustness. Although the device exhibited rigorous and reliable functionality under ambient conditions and typical human activities, comprehensive characterization of its performance under extreme environmental and mechanical conditions is essential for validating the platform for long-term, real-world monitoring applications. The study is ongoing to establish reliable, continuous, non-invasive, and clinically meaningful health monitoring systems.

Materials and methods

PDMS:PDMS–PEG preparation

The PDMS–PEG mixture was prepared by combining polydimethylsiloxane (PDMS) (Sylgard 184, Dow Corning,

MI, USA) at a 10 : 1 ratio of base to curing agent in a 50 mL conical tube. The mixture was homogenized using a planetary centrifugal mixer (Thinky Mixer ARM-310) at 2000 rpm for 2 minutes. Subsequently, a 1.5 wt% PDMS–polyethylene glycol (PEG) block copolymer solution (DBE-712, Gelest, USA; dimethylsiloxane-(60–70% ethylene oxide) block copolymer, MW 600, 20 cSt, specific gravity: 1.01, refractive index: 1.442) was added to the PDMS mixture. The combined solution was further mixed at 2000 rpm for 5 minutes to ensure uniform dispersion. The addition of the PEG block copolymer significantly increased the viscosity of the solution, necessitating thorough mixing to achieve homogeneity. Extended mixing times were employed as needed to ensure complete incorporation of the PEG block copolymer.

Soft lithography and fabrication of soft skin-interfaced microfluidics

The mold for the microfluidic device was designed using AutoCAD 2023 3D modeling software (Autodesk, USA) and fabricated using a Formlabs 3 printer with an SLA gray resin at the highest resolution setting. The microfluidic channel design features a rectangular cross-section measuring 250 μm by 250 μm, allowing a maximum capacity of 50 μL of sweat fluid for collection. Sweat containing analytes and biomarkers enters the central opening of the device, which is connected to a PDMS microchannel for collection and transport. Prior to use, the molds were cleaned sequentially with ethanol and deionized (DI) water, followed by drying with compressed air.

The fabrication of the PDMS:PDMS–PEG microfluidic devices followed a modified soft-lithography procedure, building upon standard PDMS soft-lithography techniques. The prepared mixture was poured into the cleaned molds and degassed for 30 minutes to remove air bubbles. The degassed devices were then cured in an oven at 70 °C for 5 hours or overnight to ensure complete polymerization. The devices were removed from the mold, and an inlet hole was created at the center using a 17 gauge needle. Cover films with a thickness of 750 μm were prepared using a film applicator (TQC Sheen) at a speed of 2 mm s^{-1}. These films were cast onto polyimide (PI) substrates (American Durafilm) placed on a 1/4 inch aluminum plate to ensure uniform thickness and stability and cured in an oven at 70 °C for 5 hours or overnight.

Oxygen plasma treatment was employed using a Harrick Plasma PDC-32G to create irreversible adhesion between the PDMS-based channel and cover layers. Prior to bonding, both PDMS surfaces were thoroughly cleaned and dried. The surfaces were treated with plasma exposure in an atmosphere of oxygen and nitrogen at a 1 : 5 ratio, maintained at a pressure of 0.1–0.9 Torr for 30 seconds. Immediately following plasma exposure, the treated surfaces were aligned and brought into conformal contact for 30 seconds to enable covalent bonding *via* siloxane (Si–O–Si) linkage formation.

The device assembly with semi-cured bonding was followed as described. First, the microfluidic channel layer was fabricated as described above. Separately, the cover film was prepared by casting PDMS–PEG onto polyimide (PI) substrates (American Durafilm) positioned on a 1/4 inch aluminum plate to ensure uniformity and mechanical stability. These films were cast to a thickness of approximately 750 μm and subjected to semi-curing at 70 °C for 17 minutes, creating a partially crosslinked state ideal for interfacial bonding. The cure temperature and times were optimized experimentally. Following semi-curing, the pre-cured channel layer was carefully aligned and gently placed channel-side down onto the semi-cured cover film. Care was taken to avoid deformation or undesired infiltration of uncured polymer into the microchannels. The bonded assembly was then returned to the oven for complete thermal curing at 70 °C for >5 hours or overnight to ensure full crosslinking across the interface. For devices utilizing a PI TOP/PI BOT configuration, an additional PI film was applied immediately after casting and prior to curing to encapsulate the polymer layers. Once curing was completed, devices were precisely excised from the PI backing using a circular metal cutter. To enable skin interfacing and sweat access, double-sided medical-grade tape (3M Medical Tape 1510) was applied to the inlet side of the device, and a hole punch was used to create a port for sweat entry during on-body operation.

Characterization of PDMS–PEG composite films

The water contact angles (WCAs) of PDMS–PEG films was measured using an optical tensiometer (Theta Lite, Biolin Scientific, Gothenburg, Sweden). For WCA measurements, 4 μL droplets were dispensed onto the surface of the film. The chemical structure of the PDMS–PEG and PDMS films was analyzed using a Fourier-transform infrared (FT-IR) spectrophotometer (ALPHA II, Bruker Optics Inc.) in attenuated total reflectance (ATR) mode. Samples were placed on a platinum diamond ATR crystal, and spectra were acquired over 64 scans at a resolution of 4 cm^{-1}. The optical transmittance of the fabricated films was measured over a wavelength range of 200–800 nm using a UV-vis spectrometer (Cary 60, Agilent Technologies, Santa Clara, CA, USA).

Tensile testing of the PDMS–PEG composite film

Mechanical properties were evaluated with dog-bone samples which were cut from fabricated PDMS–PEG films using a Cricut mechanical cutter. Stress–strain measurements were performed using a mechanical tester (Mark-10) system equipped with a 25 N force gauge, applying a strain rate of 0.05 mm s^{-1}.

Water vapor transmission rate measurement

The water vapor transmission rate (WVTR) of the PDMS–PEG and PDMS films was determined using permeability cups in accordance with ASTM D1653 standards. The cups,

containing a desiccant (0% relative humidity), were sealed with sample films and placed in a controlled environment. The WVTR was calculated using the following equation:

$$\mathrm{WVTR} = \frac{\Delta m}{A \times t}$$

where Δm is the mass of water loss (in mg), t is the time elapsed (h), and A is the surface area of the film exposed to moisture (in cm^2).

Threshold pressure measurement

The threshold fluid introduction pressure of the microfluidic channels was measured by recording the cross-sectional videos using the optical tensiometer while gradually increasing the pressure at a constant rate of 10 Pa min^{-1}, controlled by a microfluidic pressure control system (LineUp EZ™, Fluigent, Le Kremlin-Bicêtre, France). The film cross-section was exposed to additional light to effectively capture the meniscus movement during the pressure increase.

Capillary flowrate measurement

To evaluate spontaneous capillary-driven flow, a 15 μL droplet of deionized water was gently placed over the device inlet, which had been created with a 17 gauge needle. Care was taken to ensure the initial dispensing force did not contribute to the flow. Under these static conditions, the hydrostatic pressure exerted by the droplet's weight is estimated to be approximately 187 Pa. The subsequent fluid movement within the microchannels was recorded using a digital camera directly over the microfluidic device to determine the flowrate.

Pressurized flowrate measurement

To assess performance under active pressure, a separate experiment was conducted. The microfluidic flowrate was measured while applying a constant pressure of 1 kPa to the device inlet using the microfluidic pressure control system (LineUp EZ™, Fluigent, Le Kremlin-Bicêtre, France).

SEM image acquisition

Scanning electron microscope (SEM) images were obtained through a Zeiss Supra 55 VP field emission scanning electron microscope with an accelerating voltage of 5 kV and a working distance of 7 mm.

AFM analysis

Surface topography and roughness of the PDMS and PDMS:PDMS–PEG films were characterized using atomic force microscopy (AFM). All imaging was performed under ambient laboratory conditions in tapping mode using a Bruker Dimension Icon AFM system (Bruker, Santa Barbara, CA, USA). Scans were performed using Bruker's SNL-10 probes. For each sample, topographical images were acquired over a scan area of 1 μm by 1 μm at a scan rate of 0.5 Hz and a resolution of 256 samples per line. The raw AFM data were processed using Nanoscope Analysis software (Bruker). This software was used to apply a first-order plane-fit to correct for sample tilt, generate the 3D topographical images, and calculate the root-mean square (R_q) and arithmetic average (R_a) roughness values over the entire topographical image.

Human study physical exercise protocol and sample collection

All experiments were performed in accordance with the Guidelines of the Institutional Review Board, and experiments were approved by the ethics committee at Binghamton University. Informed consents were obtained from all human participants prior to this study (Protocol No. STUDY00003072). Written informed consent was obtained from all subjects who participated in the experiments. The designated placement of the device was cleaned with alcohol wipes before device application to minimize any foreign contamination other than the captured sweat. The non-exercise study involved subjects wearing the PDMS and PDMS:PDMS–PEG device on the forearm for an extended period, while recording activity, time, temperature, humidity, and capturing images of the microfluidic devices for estimating collected sweat volume every time interval. The exercise study consisted of aerobic and anaerobic components. Participants wore both bare PDMS and 1.5 wt% PDMS:PDMS–PEG devices on their foreheads and forearms. During aerobic exercise on the treadmill at 6 km h^{-1} speed, devices were worn for 15 minutes and then removed for collection and storage. Following a 15 minute rest period, fresh devices were reapplied to the same locations for the 15 minute anaerobic session consisting of the participants' choice of exercise with minimal aerobic respiration such as arm curls and chest press. Collected sweat samples were analyzed for pH, lactate concentration, and total sweat volume. Lactate levels were measured using assay kits (Sigma-Aldrich), pH was assessed using a Halo Wireless pH Meter with Microbulb (Hanna Instruments Inc.), and sweat volume was quantified using a microscale.

The LC-MS human study participants were recruited from a pool of volunteers within the same department. Inclusion criteria required participants to be males and females aged 18–35 years, capable of sustaining aerobic endurance for at least 40 minutes. Written informed consent was obtained from all participants prior to their involvement in the study.

Before the exercise study, participants completed a survey to assess their physiological state and dietary habits. Body composition measurements were recorded using a bioelectrical impedance analysis (BIA) device (OMRON Body Composition Monitor and Scale). Parameters measured included age, gender, height, weight, body mass index (BMI), percent body fat, percent muscle mass, resting metabolic rate (RM kcal), body age, and visceral fat (Table S3). To account

for the potential influence of diet on sweat composition, dietary intake was documented on the day of the experiment.

The study cohort consisted of four participants: one Caucasian woman, one Arabic man, and two Caucasian men, with a mean BMI of 28.83 (±5.67 standard deviation). Prior to sweat collection, the skin of the lower back was cleaned with an alcohol pad to minimize contamination. A sweat patch equipped with a microfluidic device was attached to the cleaned area. At the conclusion of the exercise session, the microfluidic device was removed and sweat collected in each chamber was extracted using a micropipette. The extracted sweat was stored in microcentrifuge tubes at −4 °C for subsequent analysis. Sweat volume was measured using a microcuvette, and microfluidic devices were single-use for each measurement to prevent cross-contamination.

Sweat was also collected directly from the skin by scooping it into a microcuvette to represent a "raw" sweat sample. The scooped sweat is centrifuged for 10 minutes at 12 000 rpm. The scooped sweat is subjected to higher contamination effects since it's from surface debris and other artifacts that can compromise its purity and accuracy for analysis. To ensure that the PEG modification is not introducing unwanted artifacts, we included a blank control, where distilled water was incubated in the PDMS–PEG device for 30 minutes.

LC-MS metabolomics and proteomics sample preparation

LC-MS metabolomics analysis was conducted using a high-performance mass spectrometer that combines trapped ion mobility spectrometry (TIMS) with time-of-flight (TOF) mass spectrometry (TimsTOF Pro2 mass spectrometer coupled with Elute UHPLC or nanoElute 2 nano-LC, Bruker). Prior to metabolomic analysis, frozen samples were thawed and centrifuged at 12 000 rpm for 5 minutes to remove particulate matter. The supernatant was diluted 30-fold and transferred into Bruker timsTOF-compatible vials for subsequent LC-MS analysis. For quantitative metabolic analysis, all chemicals and reagents were acquired of commercial origin. The analytical standard biomarkers tested were sodium L-lactate (~98%, Sigma-Aldrich®), hydrocortisone (Cor, ≥98% HPLC, Sigma-Aldrich®), and L-tryptophan (Trp, ≥98% HPLC, Sigma-Aldrich®). Standards were reconstituted with a stock solution of 1000 μL (conc: Lacta- 100 g L^{-1}; Cort- 3.54 g L^{-1}; Trp- 2.06 g L^{-1}) with serial dilutions. Prior to proteomic analysis, samples were prepared using a PreOmics iST 8x Sample Kit following the manufacturer's protocol. Protein extracts were diluted 3-fold, and protein concentrations were quantified using a Bradford Assay Kit (Bio-Rad).

Data analysis

Qualitative results used the MetaboAnalyst web-based platform (version 5.0) to assess the distribution of biomarkers across different sweat collection methods. Prior to analysis, raw LC-MS data were rigorously cleaned and filtered to remove noise, artifacts, and background signals, particularly those appearing in blank samples, which may result from instrument clogging or device contamination. Preprocessing steps such as peak picking, alignment, and normalization were applied to enhance the robustness and reproducibility of the dataset.

Proteomic analysis was conducted using liquid chromatography-mass spectrometry (LC-MS) in combination with data-independent acquisition (DIA-NN) using a Bruker Human Library. The subsequent LC-MS raw data underwent processing with DIA-NN software to facilitate protein identification and quantification. The UniProt protein database was used to understand the sequence and functional information of the detected proteins. Statistical analyses were performed using R to discern significant proteins exhibiting differential abundance between collection methods.

Author contributions

Fina Lu: conceptualization, methodology, validation, investigation, formal analysis, and writing – draft, review, and editing. Ji Hyun Yang: conceptualization, formal analysis, data curation, investigation, methodology, validation, visualization, and writing. Ahyeon Koh: conceptualization, funding acquisition, project administration, resources, supervision, validation, visualization, and writing – review and editing.

Conflicts of interest

There are no conflicts to declare.

Data availability

Human subject data used in this study are not publicly available to protect the identity of participants, according to the Binghamton University Institutional Review Board (IRB).

The data supporting this article have been included as part of the supplementary information (SI). Supplementary information is available. See DOI: https://doi.org/10.1039/d5lc00703h.

Acknowledgements

This research is also supported by the National Science Foundation (CBET #2238173) and the Small Scale Systems Integration and Packaging (S3IP) Center of Excellence. We would like to extend our special thanks to Dr. Yan Sun, Director of the Health Science Core Facility (HSCF), for the valuable discussions regarding MS analysis.

References

1 S. Kim, S. Park, J. Choi, W. Hwang, S. Kim, I.-S. Choi, H. Yi and R. Kwak, *Nat. Commun.*, 2022, **13**, 6705.
2 C.-H. Wu, H. J. H. Ma, P. Baessler, R. K. Balanay and T. R. Ray, *Sci. Adv.*, 2023, **9**, eadg4272.

3 Y. Yang and W. Gao, *Chem. Soc. Rev.*, 2019, **48**, 1465–1491.
4 N. Davis, J. Heikenfeld, C. Milla and A. Javey, *Nat. Biotechnol.*, 2024, **42**, 860–871.
5 Y. Khan, A. E. Ostfeld, C. M. Lochner, A. Pierre and A. C. Arias, *Adv. Mater.*, 2016, **28**, 4373–4395.
6 S. Cinca-Morros, S. Garcia-Rey, J. Álvarez-Herms, L. Basabe-Desmonts and F. Benito-Lopez, *Anal. Chim. Acta*, 2024, **1327**, 342988.
7 M. Bariya, H. Y. Y. Nyein and A. Javey, *Nat. Electron.*, 2018, **1**, 160–171.
8 R. Ghaffari, D. S. Yang, J. Kim, A. Mansour, J. A. Wright, Jr., J. B. Model, D. E. Wright, J. A. Rogers and T. R. Ray, *ACS Sens.*, 2021, **6**, 2787–2801.
9 A. Childs, B. Mayol, J. A. Lasalde-Ramírez, Y. Song, J. R. Sempionatto and W. Gao, *ACS Nano*, 2024, **18**, 24605–24616.
10 M. Chung, G. Fortunato and N. Radacsi, *J. R. Soc. Interface*, 2019, **16**, 20190217.
11 J. Min, J. Tu, C. Xu, H. Lukas, S. Shin, Y. Yang, S. A. Solomon, D. Mukasa and W. Gao, *Chem. Rev.*, 2023, **123**, 5049–5138.
12 J. H. Yang, U. David, Y. S. Noh and A. Koh, *Sens. Actuators, B*, 2023, **395**, 134441.
13 Y. Zhang, Y. Chen, J. Huang, Y. Liu, J. Peng, S. Chen, K. Song, X. Ouyang, H. Cheng and X. Wang, *Lab Chip*, 2020, **20**, 2635–2645.
14 W. Liu, H. Cheng and X. Wang, *npj Flexible Electron.*, 2023, **7**, 43.
15 T. Saha, R. Del Caño, K. Mahato, E. De la Paz, C. Chen, S. Ding, L. Yin and J. Wang, *Chem. Rev.*, 2023, **123**, 7854–7889.
16 S. Cho, S. M. Shaban, R. Song, H. Zhang, D. Yang, M.-J. Kim, Y. Xiong, X. Li, K. Madsen, S. Wapnick, S. Zhang, Z. Chen, J. Kim, G. Guinto, M. Li, M. Lee, R. F. Nuxoll, S. Shajari, J. Wang, S. Son, J. Shin, A. J. Aranyosi, D. E. Wright, T.-i. Kim, R. Ghaffari, Y. Huang, D.-H. Kim and J. A. Rogers, *Sci. Transl. Med.*, 2024, **16**, eado5366.
17 D. R. Seshadri, R. T. Li, J. E. Voos, J. R. Rowbottom, C. M. Alfes, C. A. Zorman and C. K. Drummond, *NPJ Digit. Med.*, 2019, **2**, 72.
18 G. M. Whitesides, *Nature*, 2006, **442**, 368–373.
19 K. Raj M. and S. Chakraborty, *J. Appl. Polym. Sci.*, 2020, **137**, 48958.
20 Z. Wang, A. Shah, H. Lee and C. H. Lee, *Lab Chip*, 2025, **25**, 4542–4576.
21 L. B. Baker, J. B. Model, K. A. Barnes, M. L. Anderson, S. P. Lee, K. A. Lee, S. D. Brown, A. J. Reimel, T. J. Roberts, R. P. Nuccio, J. L. Bonsignore, C. T. Ungaro, J. M. Carter, W. Li, M. S. Seib, J. T. Reeder, A. J. Aranyosi, J. A. Rogers and R. Ghaffari, *Sci. Adv.*, 2020, **6**, eabe3929.
22 A. Koh, D. Kang, Y. Xue, S. Lee, R. M. Pielak, J. Kim, T. Hwang, S. Min, A. Banks, P. Bastien, M. C. Manco, L. Wang, K. R. Ammann, K.-I. Jang, P. Won, S. Han, R. Ghaffari, U. Paik, M. J. Slepian, G. Balooch, Y. Huang and J. A. Rogers, *Sci. Transl. Med.*, 2016, **8**, 366ra165.
23 S. Jo and K. Park, *Biomaterials*, 2000, **21**, 605–616.
24 D. B. Mair, M. A. C. Williams, J. F. Chen, A. Goldstein, A. Wu, P. H. U. Lee, N. J. Sniadecki and D.-H. Kim, *ACS Appl. Mater. Interfaces*, 2022, **14**, 38541–38549.
25 A. Gökaltun, Y. B. Kang, M. L. Yarmush, O. B. Usta and A. Asatekin, *Sci. Rep.*, 2019, **9**, 7377.
26 A. Fatona, Y. Chen, M. Reid, M. A. Brook and J. M. Moran-Mirabal, *Lab Chip*, 2015, **15**, 4322–4330.
27 J. Heikenfeld, A. Jajack, B. Feldman, S. W. Granger, S. Gaitonde, G. Begtrup and B. A. Katchman, *Nat. Biotechnol.*, 2019, **37**, 407–419.
28 R. F. R. Ursem, A. Steijlen, M. Parrilla, J. Bastemeijer, A. Bossche and K. De Wael, *Lab Chip*, 2025, **25**, 1296–1315.
29 T. Saha, T. Songkakul, C. T. Knisely, M. A. Yokus, M. A. Daniele, M. D. Dickey, A. Bozkurt and O. D. Velev, *ACS Sens.*, 2022, **7**, 2037–2048.
30 T. Saha, M. I. Khan, S. S. Sandhu, L. Yin, S. Earney, C. Zhang, O. Djassemi, Z. Wang, J. Han, A. Abdal, S. Srivatsa, S. Ding and J. Wang, *Adv. Sci.*, 2024, **11**, 2405518.
31 H. Y. Y. Nyein, M. Bariya, B. Tran, C. H. Ahn, B. J. Brown, W. Ji, N. Davis and A. Javey, *Nat. Commun.*, 2021, **12**, 1823.
32 S. Shin, R. Liu, Y. Yang, J. A. Lasalde-Ramírez, G. Kim, C. Won, J. Min, C. Wang, K. Fan, H. Han, C. Uwakwe, W. Heng, T. K. Hsiai, Z. Li, J. D. FitzGerald and W. Gao, *Sci. Adv.*, 2025, **11**, eadw9024.
33 F. Lorestani, X. Zhang, A. M. Abdullah, X. Xin, Y. Liu, M. M. Rahman, M. A. S. Biswas, B. Li, A. Dutta, Z. Niu, S. Das, S. Barai, K. Wang and H. Cheng, *Adv. Funct. Mater.*, 2023, **33**, 2306117.
34 F. Lorestani, X. Zhang, Z. Ataie, A. Kedzierski, Y. Liu, A. López, A. Dutta, K. Kacala, Z. Niu, A. Sheikhi and H. Cheng, *Small*, 2025, **21**, 2502655.
35 Z. Sonner, E. Wilder, J. Heikenfeld, G. Kasting, F. Beyette, D. Swaile, F. Sherman, J. Joyce, J. Hagen, N. Kelley-Loughnane and R. Naik, *Biomicrofluidics*, 2015, **9**, 031301.
36 L. M. Schmidt-Speicher and K. Länge, *Curr. Opin. Electrochem.*, 2021, **29**, 100755.
37 G. Ertürk and B. Mattiasson, *Sensors*, 2017, **17**, 288.
38 A. Golparvar, L. Thenot, A. Boukhayma and S. Carrara, *Biosensors*, 2024, **14**, 12.
39 Y. Sekine, S. B. Kim, Y. Zhang, A. J. Bandodkar, S. Xu, J. Choi, M. Irie, T. R. Ray, P. Kohli, N. Kozai, T. Sugita, Y. Wu, K. Lee, K.-T. Lee, R. Ghaffari and J. A. Rogers, *Lab Chip*, 2018, **18**, 2178–2186.
40 A. Camós Noguer, R. Latipov, F. B. Madsen, A. E. Daugaard, S. Hvilsted, S. M. Olsen and S. Kiil, *Prog. Org. Coat.*, 2018, **120**, 179–189.
41 M. Razavifar, A. Abdi, E. Nikooee, O. Aghili and M. Riazi, *Sci. Rep.*, 2025, **15**, 16611.
42 J. Shin, J. W. Song, M. T. Flavin, S. Cho, S. Li, A. Tan, K. R. Pyun, A. G. Huang, H. Wang, S. Jeong, K. E. Madsen, J. Trueb, M. Kim, K. Nguyen, A. Yang, Y. Hsu, W. Sung, J. Lee, S. Phyo, J.-H. Kim, A. Banks, J.-K. Chang, A. S. Paller, Y. Huang, G. A. Ameer and J. A. Rogers, *Nature*, 2025, **640**, 375–383.
43 Z. Xu, Y. Liu, M. Lv, X. Qiao, G.-C. Fan and X. Luo, *Anal. Chim. Acta*, 2023, **1283**, 341948.